

Simulations of minor mergers. I. General properties of thick disks

Álvaro Villalobos^{*} and Amina Helmi[†]

Kapteyn Astronomical Institute, University of Groningen, P.O. Box 800, 9700 AV Groningen, The Netherlands

ABSTRACT

We present simulations of the formation of thick disks via the accretion of two-component satellites onto a pre-existing thin disk. Our goal is to establish the detailed characteristics of the thick disks obtained in this way, as well as their dependence on the initial orbital and internal properties of the accreted objects. We find that mergers with 10–20% mass of the mass of the host lead to the formation of thick disks whose characteristics are similar, both in morphology as in kinematics, to those observed. Despite the relatively large mass ratios, the host disks are not fully destroyed by the infalling satellites but they are considerably tilted, heated up and flared. The final scale-heights of the disks depend both on the initial inclination and properties of the merger, but the fraction of satellite stellar particles at ~ 4 scale-heights directly measures the mass ratio between the satellite and host galaxy. A robust prediction of the minor merger scenario for the formation of thick disks is the presence of boxy contours at very low surface brightness levels ($\Sigma_V \sim 28$ mag/arcsec²). Kinematically, the velocity ellipsoids of the simulated thick disks are consistent with observations at the solar radius in the Galaxy. The trend of σ_Z/σ_R with radius is found to be a very good discriminant of the initial inclination of the decaying satellite. In the Milky Way, the possible existence of a vertical gradient in the rotational velocity of the thick disk as well as the observed value of σ_Z/σ_R at the solar vicinity appear to favour the formation of the thick disk by a merger with either low or intermediate orbital inclination.

Key words: methods: numerical – galaxies: formation, kinematics and dynamics, structure – Galaxy: disc, kinematics and dynamics, formation

1 INTRODUCTION

The different components of disk galaxies contain key information about various stages of the formation history of these systems. In this sense, one of the most significant components for studying signatures of galaxy formation are the thick disks because they contain imprints of the state of early disks and their interaction with the galactic environment (Freeman & Bland-Hawthorn 2002).

Until now thick-disks have been detected in S0 galaxies (Burstein 1979; Tsikoudi 1979), in the Milky Way (Gilmore & Reid 1983) and in many other spirals (van der Kruit & Searle 1981a,b; Jensen & Thuan 1982; van Dokkum et al. 1994; Morrison et al. 1997; Pohlen et al. 2000; Dalcanton & Bernstein 2002; Yoachim & Dalcanton 2006, and references therein). As such, thick disks appear to be a rather ubiquitous structural component of galaxies.

Historically, there have been two types of scenarii pro-

posed to explain the formation of thick disks: (i) “dissipational”, and (ii) “predominantly dissipationless” models. In the first case, thick-disk stars are formed during the dissipational collapse of gas with a large scale-height, after the halo has formed and before the thin disk has completely collapsed. A variant of this model, more in line with modern cosmology, is given by Brook et al. (2004, 2005) and consists of the formation of the thick disk in an epoch of multiple mergers of gas-rich building blocks. In this class of models, one may expect a smooth transition between properties of the thin and thick disks (Eggen et al. 1962; Gilmore & Wyse 1986; Norris & Ryan 1991; Burkert et al. 1992; Pardi et al. 1995; Fuhrmann 2004). In the “predominantly dissipationless” models the thick disk stars were either: (1) vertically “heated” from a pre-existent thin disk during a (significant) minor merger (Quinn et al. 1993; Mihos et al. 1995; Walker et al. 1996; Robin et al. 1996; Velázquez & White 1999; Aguerri et al. 2001; Chen et al. 2001); (2) directly deposited at large scale-heights as tidally stripped debris during the accretion of smaller satellite galaxies (Bekki & Chiba 2001; Gilmore et al. 2002; Abadi et al. 2003; Martin et al.

^{*} E-mail: villalobos@astro.rug.nl

[†] E-mail: ahelmi@astro.rug.nl

2004; Navarro et al. 2004; Brook et al. 2004; Wyse et al. 2006); or (3) the product of the dissolution of massive thin-disk clusters with small radii and large velocity dispersions (Kroupa 2002). The first and third models require the presence of a pre-existing thin disk. In this second class of models, the thick disk may be characterised as a completely foreign component.

Models involving either one or more minor mergers – including the case of gas-rich accretion proposed by Brook et al. – are natural in the context of current theories of hierarchical structure formation (e.g., Kazantzidis et al. 2007). Such models are also supported by modern studies of both kinematical and chemical properties of the Milky Way and external galaxies (Yoachim & Dalcanton 2005, 2006; Seth et al. 2005; Mould 2005; Elmegreen & Elmegreen 2006). The observed lack of vertical colour and chemical gradients, as well as the presence of counter-rotating disks, favours scenarios in which thin and thick disks formed as separate entities. However, it is unclear to what extent such models reproduce the detailed properties of observed thick disks. For example, in the dissipationless minor merger scenario, the thick disk should contain stars from both the heated thin disk and the accreted satellite. What fraction of the stars come from each constituent? If they are mostly satellite debris, one may expect a significantly metal-poor thick disk, which appears to be inconsistent with the observations reported in, e.g., Mould (2005).

It is the lack of very detailed predictions that motivates us to revisit the problem of thick disk formation. In this paper, we explore the hypothesis of the heating of a pre-existing thin disk by a single minor merger, and study the global properties of the final product. In a follow-up paper we will focus on its phase-space structure with the aim of making a detailed comparison to the thick disk in the Solar neighbourhood. In paper II we also develop the intuition needed to uncover the debris from the object that may have triggered its formation.

Significant work has been carried out in the past to model the disk heating process by a minor merger from the numerical point of view, starting from Quinn & Goodman (1986) (QG86); Quinn, Hernquist & Fullagar (1993) (QHF93); Mihos et al. (1995); Walker, Mihos & Hernquist (1996) (WMH96); Huang & Carlberg (1997) (HC97); Sellwood et al. (1998); upto Velázquez & White (1999) (VW99). Their work has essentially shown that it is relatively easy to produce thick disks whose general properties are consistent with those observed. However, we believe there is still room for improvement, both in the initial conditions used to model this process (see also Kazantzidis et al. 2007), as well as in the degree of detail necessary for comparisons to the latest observations of thick disks.

The initial conditions space is very large, and it is not desirable to probe it randomly. We have therefore made the following physically motivated choices. (i) We model the formation of thick disks at two different redshifts, by scaling the properties of the host galaxy and accreted satellite according to cosmological models, as in Mo, Mao & White (1998) (ii) We consider the accretion of relatively massive satellites (10% or 20% mass ratios), embedded in dark-matter halos, and with stellar distributions that are initially either spherical (and on the fundamental plane of dE+dSphs galaxies)

or disk. (iii) The satellites are released much farther away from the host disk compared to previous studies, and their orbits are consistent with those of infalling substructures in cosmological simulations (e.g., Benson 2005).

The outline of this paper is the following: In §2 we describe in detail the numerical procedure used to build self-consistently the different components of both the host galaxy and satellites including our choices for the numerical parameters and the orbital parameters of the satellites. §3 describes the outcome of the simulations, focusing on the final properties of thick disks and the evolution of satellites. In §4 we present a discussion and limitations of our approach. In §5 we summarise the main results.

2 SETTING UP THE SIMULATIONS

In this section, we describe in detail the procedure adopted to model the host disk galaxy and the (to be accreted) satellite. We consider two configurations: a merger with a host whose properties resemble the Milky Way today (our “z=0” experiment), and a merger with a smaller host disk galaxy (this is our “z=1” experiment). The “z=0” configuration has been often used in the past in the same context (QG86; QHF93; WMH96; HC97; VW99; Aguerrí et al. 2001; Font et al. 2001; Ardi et al. 2003; Hayashi & Chiba 2006). In the “z=1” configuration both the host system and the satellite’s properties are scaled to those expected at z=1 according to the model of Mo et al. (1998). In this case, the aim is to simulate the merger event that might have given rise to the Milky Way thick disk. In this configuration the mass of the present-day thick disk of the Milky Way is roughly equal to the combined mass of the host disk galaxy and the stellar component of the satellite.

In this section we also describe the orbital parameters of the various experiments. Furthermore, we explain the choices made for the numerical parameters employed in our simulations, and describe the global stability of the system.

2.1 Main disk galaxy

We model the main disk galaxy as a self-consistent two-component system, containing a dark matter halo and a stellar disk.

2.1.1 Dark Matter Halo

The dark matter (DM) halos in our simulations follow a NFW mass density profile (Navarro, Frenk & White 1996, 1997, hereafter NFW):

$$\rho_{NFW}(r) = \frac{\rho_s}{(r/r_s)(1+r/r_s)^2} \quad (1)$$

where ρ_s is a characteristic scale density and r_s a scale radius. The advantage of using this density profile is that it is consistent with cosmological simulations, and its evolution with redshift (or time) is relatively well-known (e.g., Wechsler et al. 2002). This implies that it is easy to re-scale its properties to study the formation of thick disks at redshifts greater than zero.

In this paper we adopt a flat cosmology defined by $\Omega_m(z=0) = 0.3$ and $\Omega_\Lambda = 0.7$ with a Hubble constant of $H(z=0) = 70$ km/s/Mpc.

The virial radius of the halo $R_{vir}(z)$ is defined as the radius within which the mean density is $\Delta_{vir}(z)$ times the critical density $\rho_c(z)$ of the universe at a given redshift:

$$M_{vir}(z) = \frac{4\pi}{3} \Delta_{vir}(z) \rho_c(z) R_{vir}^3 \quad (2)$$

where the virial overdensity $\Delta_{vir}(z)$ is taken from the solution to the dissipationless collapse in the spherical top-hat model (Peebles 1980; Eke, Cole & Frenk 1996). Its value is $18\pi^2$ for a critical universe but has a dependency on cosmology. In the case of flat cosmologies, $\Delta_{vir}(z) \approx (18\pi^2 + 82x + 39x^2)$, where $x = \Omega(z) - 1$, and $\Omega(z)$ is defined as the ratio between mean matter density and critical density at redshift z (Bryan & Norman 1998). Another important related quantity is the concentration c defined as $c = R_{vir}/r_s$. From Wechsler et al. (2002) we take the relation linking M_{vir} to the concentration parameter c at redshift $z=0$ as:

$$c \simeq 20 \left(\frac{M_{vir}}{10^{11} M_\odot} \right)^{-0.13} \quad (3)$$

We follow Wechsler et al. (2002) and Zhao et al. (2003) to scale both the virial mass of the halo and its concentration as a function of redshift:

$$M_{vir}(z) = M_{vir}(z=0) \exp(-2a_c z), \quad (4)$$

$$c(z) = \frac{c(z=0)}{1+z} \quad (5)$$

where a_c is a constant defined as the formation epoch of the halo, taken as $a_c = 0.34$. In practice this means that the structure of the halo of the main galaxy at any redshift is fully determined by imposing only a value for the virial mass at redshift $z=0$. The values of the halo parameters used in our simulations are included in the Table 1.

Since the mass of a NFW profile formally diverges with radius, we introduce an exponential truncation starting at R_{vir} and decaying on a scale r_{dec} (Springel & White 1999):

$$\rho(r) = \frac{\rho_s}{c(1+c)^2} \left(\frac{r}{R_{vir}} \right)^\epsilon \exp\left(-\frac{r-R_{vir}}{r_{dec}}\right) \quad (r > R_{vir}) \quad (6)$$

where r_{dec} is a free parameter. By requiring continuity at R_{vir} between Eqs. (1) and (6), and also between their logarithmic slopes, the exponent ϵ is computed as:

$$\epsilon = -\frac{1-3c}{1+c} + \frac{R_{vir}}{r_{dec}}. \quad (7)$$

Note that for $r_{dec} = 0.1R_{vir}$ the total mass of the halo becomes $\sim 10\%$ larger than M_{vir} . We define the maximum extension of the halo as $R_{max} = R_{vir} + 3r_{dec}$.

We also allow the contraction of the halo in response to the formation of a stellar disk in its central part (Blumenthal et al. 1986; Mo et al. 1998). The adiabatic contraction first assumes that the gas (that later forms the disk/bulge) is distributed in the same way as the dark matter. Then both the spherical symmetry of the halo and also the angular momentum of each dark matter orbit are conserved during the contraction, i.e.,:

$$r_i M_i(r_i) = r_f M_f(r_f) \quad (8)$$

where r_i and r_f are the initial and final radius of a shell of dark matter, M_i is the initial total mass (distributed according to an NFW profile) and M_f is the mass distribution after the disk has been formed, and also includes the contribution of the disk. Therefore,

$$M_f(r_f) = M_d(r_f) + (1 - m_d) M_i(r_i) \quad (9)$$

where $m_d = M_{disk}/M_{halo}$. The final dark matter distribution of the adiabatically concentrated halo will be:

$$M_{halo}(r) = M_f(r) - M_{disk}(r). \quad (10)$$

Now that the mass distribution of the halo component has been defined, it is straightforward to initialise the positions of the particles in our halos. As the next step, the velocity of each particle is computed from the distribution function (DF) associated to the adiabatically contracted mass density profile $\rho_{halo}(r)$. We follow Kazantzidis et al. (2004) and compute numerically the DF that, in general, is given by¹:

$$f(Q) = \frac{1}{\sqrt{8}\pi^2} \left[\int_0^Q \frac{d^2 \rho_{halo}}{d\psi^2} \frac{d\psi}{\sqrt{Q-\psi}} + \frac{1}{\sqrt{Q}} \left(\frac{d\rho_{halo}}{d\psi} \right)_{\psi=0} \right] \quad (11)$$

(Eddington 1916; Binney & Tremaine 1987) where $Q = \psi - v^2/2$; $\psi = -\Phi(r)$ is the effective gravitational potential (including the disk); and v is the velocity of each particle. Finally, we use the rejection method (Press et al. 1992) to generate the velocities for our particles.

2.1.2 Stellar Disk

The disk component is constructed following the procedure outlined by QHF93 and Hernquist (1993) which consists, briefly, in initialising particle positions according to a density profile of the form:

$$\rho_d(R, z) = \frac{M_d}{8\pi R_D^2 z_0} \exp\left(-\frac{R}{R_D}\right) \text{sech}^2\left(\frac{z}{2z_0}\right) \quad (12)$$

where M_d is the disk mass, R_D is the exponential scale-length, and z_0 is the exponential² scale-height.

The velocity components v_R , v_ϕ and v_z of the disk particles are calculated from moment equations of the collisionless Boltzmann equation (CBE) supplemented by observational constraints (Binney & Tremaine 1987). We assume that locally (at each point in the disk) the velocity distribution can be approximated by a Maxwellian, whose parameters are set up as follows:

- The radial velocity dispersion $\overline{v_R^2}(R) \propto \exp(-R/R_D)$. This is motivated by observations of external galaxies (van der Kruit & Searle 1981a; Lewis & Freeman 1989). The normalisation constant is set by adopting a certain value of the stability Q-parameter (Toomre 1964) at a particular location in the disk. In this paper $Q = 2$ at $R = 2.4R_D$, which for a Milky Way-like disk corresponds to the solar radius.

¹ For a spherical non-rotating system.

² Note that $\text{sech}^2(z/2z_0) \approx \exp(-z/z_0)$ for $z \gg z_0$.

Table 1. Properties of host disk galaxies.

| | “z=0” | “z=1” | |
|-----------------------------------|----------------------|-----------------------|---------------|
| NFW Halo | | | |
| Virial mass, M_{vir} | 10^{12} | 5.07×10^{11} | $[M_{\odot}]$ |
| Virial radius, R_{vir} | 258.91 | 122.22 | [kpc] |
| Concentration, c | 13.12 | 6.56 | |
| Circular velocity, $V_c(R_{vir})$ | 129.17 | 133.87 | [km/s] |
| N_H | 500000 | 500000 | |
| Softening, ϵ_{halo} | 0.35 | 0.41 | [kpc] |
| Disk | | | |
| Disk mass, M_{disk} | 2.8×10^{10} | 1.2×10^{10} | $[M_{\odot}]$ |
| Scale-length, R_D | 3.5 | 1.65 | [kpc] |
| Scale-height, z_0 | 0.35 | 0.165 | [kpc] |
| Toomre $Q(R = 2.4R_D)$ | 2.0 | 2.0 | |
| N_D | 100000 | 100000 | |
| Softening, ϵ_{disk} | 0.05 | 0.012 | [kpc] |

• The vertical velocity dispersion $\overline{v_z^2}(R) = 2\pi G \Sigma(R) z_0$, following the isothermal sheet model (Spitzer 1942).

• The dispersion in the azimuthal direction is obtained by using the epicyclic approximation (Binney & Tremaine 1987) $\sigma_{\phi}^2(R) = \overline{v_R^2}(R) \kappa^2(R) / 4\Omega^2(R)$, where κ and Ω are the epicyclic and angular frequencies, respectively. The mean values of the azimuthal Gaussian distributions are calculated from the second moment of the CBE,

$$\overline{v_{\phi}^2}(R) = \overline{v_R^2}(R) \left[1 - \frac{\kappa^2(R)}{4\Omega^2(R)} - 2 \frac{R}{R_D} \right] + v_c^2(R),$$

where $v_c(R) = R \Omega(R)$ is the circular velocity considering all the components of the system.

Note that velocities derived from the CBE are close but not identical to the ones derived from the DF of the disk. Unfortunately, the DF is unknown for the disk in Eq. (12). Therefore, we can expect some initial evolution in the disk properties. We shall see in §2.5 that this evolution is indeed minimal.

Following Mo et al. (1998), the ratios M_{halo}/M_{disk} and R_{vir}/R_D have been kept nearly constant for all redshifts. The scale-height z_0 has been kept as $0.2R_D$ according to observations of external galaxies (Kregel et al. 2002). This has also been assumed in our “z=1” experiments. By keeping this ratios constant, the way in which the mass and dimensions of the disk component scale with redshift is simplified, since it follows the same scaling with redshift as the halo within which it is embedded. The chosen values of disk parameters are listed in Table 1 for our “z=0” and “z=1” experiments.

2.2 Satellite Galaxies

The satellite galaxies are designed self-consistently with both a dark matter and a stellar components. The dark halo follows a NFW density profile, and the initialisation procedure is identical to that outlined in §2.1.1.

We consider two possible stellar distributions: an exponential disk (as in §2.1.2), and a spherical Hernquist bulge. In this case, the density is given by (Hernquist 1990):

Table 2. Properties of satellite galaxies.

| | “z=0” | “z=1” | |
|-----------------------------------|--------------------|------------------------|---------------|
| NFW Halo | | | |
| Virial mass, M_{vir} | 2×10^{11} | 1.01×10^{11} | $[M_{\odot}]$ |
| Virial radius, R_{vir} | 151.40 | 71.35 | [kpc] |
| Concentration, c | 16.18 | 8.09 | |
| Circular velocity, $V_c(R_{vir})$ | 75.50 | 78.10 | [km/s] |
| N_H | 100000 | 100000 | |
| Softening, ϵ_{halo} | 0.14 | 0.07/0.14 ¹ | [kpc] |
| Disk | | | |
| Disk mass, M_{disk} | 5.6×10^9 | 2.4×10^9 | $[M_{\odot}]$ |
| Scale-length, R_D | 1.69 | 0.96 | [kpc] |
| Scale-height, z_0 | 0.17 | 0.095 | [kpc] |
| Toomre $Q(R = 2.4R_D)$ | 2.0 | 2.0 | |
| N_D | 100000 | 100000 | |
| Softening, ϵ_{disk} | 0.024 | 0.007 | [kpc] |
| Bulge | | | |
| Bulge mass, M_{bulge} | 5.6×10^9 | 2.4×10^9 | $[M_{\odot}]$ |
| Scale radius, a_b | 0.9 | 0.709 | [kpc] |
| Velocity dispersion, σ_0 | 96.29 | 69.06 | [km/s] |
| N_B | 100000 | 100000 | |
| Softening, ϵ_{bulge} | 0.07 | 0.07 | [kpc] |

¹: Softenings used in disk and spherical satellites respectively.

$$\rho_b(r) = \frac{M_b}{2\pi} \frac{a_b}{r(r+a_b)^3} \quad (13)$$

where M_b is the bulge mass and a_b is the scale radius. Since the DF for the Hernquist model is analytic, initialisation is straightforward.

Both types of satellites satisfy $M_{total,sat} = 0.2M_{total,host}$ for the “z=0” and “z=1” experiments. In particular, the mass ratio between dark matter and luminous matter in the satellites is set to be the same as in the host galaxy. This implies that the mass of the stellar components of our satellites is 20% of $M_{disk,host}$, similar to those adopted in previous work on disk heating by satellite accretion (QHF93; WMH96; HC97; VW99). Note however that the initial total mass of the satellite is comparable to that of the host disk. For completeness, we also include the case of a satellite with a stellar mass of 10% of $M_{disk,host}$. In this case the total mass of the satellite is also 10% of that of the host galaxy.

The spherical satellites lie on the observed fundamental plane of dE+dSphs galaxies (de Rijcke et al. 2005):

$$\log L_B \sim 4.39 + 2.55 \log \sigma_0 \quad (14)$$

$$\log L_B \sim 8.65 + 3.55 \log R_e \quad (15)$$

where L_B is the blue-band luminosity, and σ_0 is the central velocity dispersion. The effective radius is related to the scale radius by $R_e \approx 1.82a_b$ for a Hernquist density profile (Hernquist 1990). Finally, we fix the mass-to-light ratio $\Upsilon_B = 2$ (Binney & Merrifield 1998) to derive the stellar mass of our spherical satellites.

The structural parameters of the disk satellites, R_D and z_0 are set as follows. The scale-length is defined by keeping the same ratio R_{vir}/R_D as in the host. As before

the scale-height of the disk is related to the scale-length by $z_0 = 0.2R_D$.

The above relations fully specify the properties of our satellites, both for the “z=0” and “z=1” experiments. Note that the variation with redshift is always linked to that of the host halo. Table 2 include the properties of disk satellites for “z=0” and “z=1”.

2.3 Orbital Parameters

We release our satellites from significantly larger distances than previous works (e.g., QG86; VW99; Kazantzidis et al. 2007). For the “z=0” case, the satellite is launched from the virial radius of the host galaxy computed at z=1 ($R_{vir} = 122.22$ kpc $\approx 35R_D$). For the “z=1” experiment, it is launched from a distance of 83.9 kpc ($\approx 50R_D$) which corresponds to the virial radius of the host galaxy computed at z=1.6.

To initialise the orbital velocities of the satellites, we follow Benson (2005). Benson determined the orbital parameters of DM substructures at the time they crossed the virial radius of their host halos (see also Tormen 1997; Vitvitska et al. 2002; Khochfar & Burkert 2006). We choose for the velocities of our satellites the most probable values of the distributions as given for z=0 (since little variation is visible as a function of redshift). The radial and tangential velocity distributions peak, respectively, at 0.9 and 0.6 in units of $V_c(R_{vir})$.

We consider for our satellites initial orbital inclinations of 0°, 30° and 60° (with respect to the plane of the host disk), in both prograde and retrograde directions with respect to the rotation of the host disk. Table 3 summarises the orbital parameters adopted for both spherical and disk satellites, for the configurations at “z=0”, and “z=1”.

Note that within each configuration, all the satellites are initially released from the same distance with the same velocity modulus, i.e., they all have the same total energy and modulus of the angular momentum, but the latter varying its orientation. This implies that the initial apocentre, pericentre (and hence orbital eccentricity) are the same for all experiments. However, as we shall see in §3.1 the orbits evolve due to dynamical friction, with some dependence on the internal properties of the satellite. Therefore, at the time the satellite merges with the disk, the orbits of all our experiments are different.

With these initial conditions, we find that our satellites have completely merged with the host disks by z \approx 0.4 and by z \approx 1, respectively for the “z=0” and “z=1” cases.

2.4 Numerical Parameters

The N -body systems are evolved using Gadget-2.0 (Springel 2005) a well documented massively parallel TreeSPH code. Depending on the system under study, this code has to be provided with suitable values for the so-called numerical parameters, being these: the number of particles N to represent a given component in the system; the softening ϵ of gravitational forces to avoid strong artificial accelerations between particles passing close to each other; and finally the timestep Δt , that controls the frequency at which positions and velocities are computed for each particle. In general, these three

Table 3. Initial orbital parameters of satellite galaxies.

| i | x | z | v_x | v_z | L_z |
|-------|-------|-------|--------|--------|---------|
| “z=0” | | | | | |
| 0° | 122.2 | 0.0 | -137.7 | 0.0 | 11219.8 |
| 30° | 105.8 | 61.1 | -119.2 | -68.8 | 9716.6 |
| 60° | 61.1 | 105.8 | -68.8 | -119.2 | 5609.9 |
| “z=1” | | | | | |
| 0° | 83.9 | 0.0 | -118.2 | 0.0 | 6615.9 |
| 30° | 72.7 | 42.0 | -102.4 | -59.1 | 5729.5 |
| 60° | 42.0 | 72.7 | -59.1 | -102.4 | 3307.9 |

NOTES:

- Distances in kpc, velocities in km/s, angular momentum in kpc \times km/s.
- In all cases, $y = 0$ kpc, and $v_y = 91.8$ km/s for “z=0” and $v_y = 78.8$ km/s for “z=1”.
- Listed v_y and L_z are for prograde orbits. Retrograde orbits have the opposite sign.
- Initially $r_{apo} = 77$ kpc and 49 kpc, $r_{peri} \sim 10$ kpc and 5 kpc, respectively for the “z=0” and “z=1” configurations (as measured from the first apocentre and the subsequent pericentre). The corresponding eccentricities $e = (r_{apo} - r_{peri}) / (r_{apo} + r_{peri})$ are 0.77 and 0.82.

parameters set the mass, spatial and time resolution in a numerical simulation. At the moment of defining N , ϵ and Δt the usual problem is that they are interrelated in a complicated way. For instance, N will depend on the available CPU power to run the simulations; ϵ will depend on both N and the mass distribution of the system to be simulated; and Δt will depend on the smallest spatial resolution that is possible to resolve, ϵ , and again on the available CPU power. The optimal choice of these parameters will establish a compromise between quality and efficiency in a numerical simulation.

2.4.1 Number of particles

Tables 1 and 2 list the numbers of particles used for each component in our simulations. As shown by WMH96, using self-consistent simulations of an isolated halo-disk system, large numbers of particles in the halo are needed to suppress the formation of bar perturbations in the disk. This is because large N_{halo} decreases the graininess of the potential, which bars are seeded from. WMH96 suggest the use of ~ 500000 particles in the halo in order to smooth out the potential for time scales comparable to the orbital decay of satellites in our simulations.

For our purposes, bars are an unwanted effect because they represent an additional source of disk heating, besides the one of interest here. Although the complete elimination of bar formation in a self-consistent simulation is difficult, its effect on the disk can be constrained by evolving the main disk galaxy in isolation, for a comparable timescale as the merger simulation.

The number of particles in the host disk $N_{host,disk} = 10^5$, and is similar to previous studies on disk heating by mergers with satellites. The satellites are modeled with a relatively large number of particles (particularly in comparison

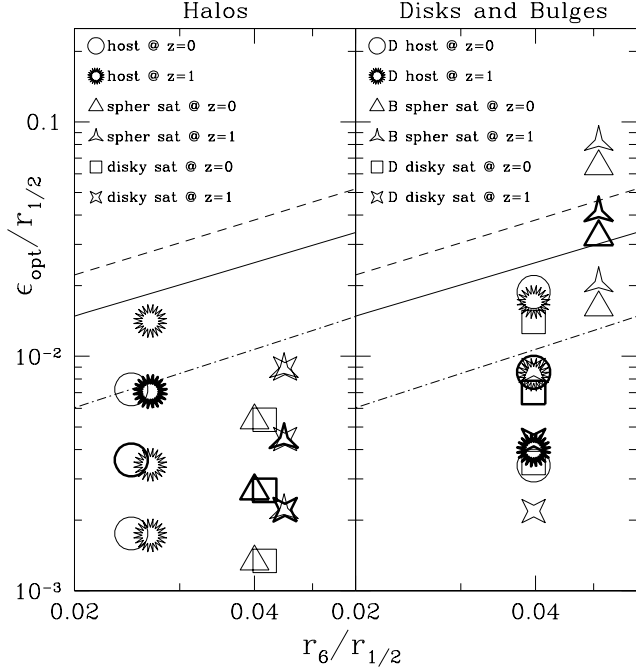


Figure 1. Numerical softening as a function of the mean distance from each particle to the 6th closest neighbour in units of the half-mass radius $r_{1/2}$. Straight lines are extrapolations towards smaller r_6 taken from the results of Athanassoula et al. (2000) [see Fig. 11 in that work]. Dashed, solid and dot-dashed lines show the values for a homogeneous, Plummer and Dehnen sphere (with $\gamma = 0$), respectively. The symbols indicate the values of softenings explored in this paper for each component. Darker symbols show the optimal softenings that produced the best stability in each case.

to previous works) to follow the distribution of the debris, which is the focus of Paper II. In all cases we can follow accurately the structure and evolution of each component during the simulations.

2.4.2 Softening

Many studies have been carried out on how to choose the optimal gravitational force softening ϵ in order to faithfully represent the system (see Sellwood 1987, for an excellent review). We use here the prescription by Athanassoula et al. (2000). These authors present a simple method to estimate ϵ for arbitrary mass distributions as a function of the number of particles. The optimal softening ϵ_{opt} is the one that minimises the error in the forces between particles in a system with a given mass distribution. They find a correlation between ϵ_{opt} and the distance $r_{6,mean}$ from every particle to its sixth closest neighbour, which is defined as:

$$r_{6,mean} = \left(N^{-1} \sum_{i=1}^N r_{6,i}^{-1} \right)^{-1} \quad (16)$$

where $r_{6,mean}$ depends on both the number of particles and the mass distribution. Fig. 1 shows ϵ_{opt} as a function of $r_{6,mean}$ for three mass distributions discussed by Athanassoula et al. (2000) in order of increasing density: homogeneous sphere, Plummer profile and Dehnen model

(with $\gamma = 0$). To estimate the ϵ_{opt} for the systems of our simulations the procedure followed is: 1) compute $r_{6,mean}$ for each of our components; 2) compare the central density of our components to the ones of the homogeneous, Plummer and Dehnen spheres. By doing so the optimal softening for each component can be constrained within a range on the plane $r_6 - \epsilon_{opt}$; and 3) ϵ_{opt} is found by running a few simulations with a set of ϵ within this range and choosing the one that offers the best stability. Specifically, a softening is considered optimal when each component of both the host and satellite systems present the least evolution in their structure and kinematics (in the case of the host minimising the effect of non-axisymmetries) during the amount of time required for the satellite to sink and become fully disrupted.

In Fig. 1 darker symbols show the values of ϵ_{opt} for each component at every redshift. Note that for each component the values of ϵ_{opt} are well constrained on the $r_6 - \epsilon_{opt}$ plane, facilitating the extrapolation of these optimal values to similar systems with a different number of particles. For each component, the adopted values of ϵ_{opt} are listed in Table 1 and Table 2.

The distinctive location of the optimal softenings on the $r_6 - \epsilon_{opt}$ diagram basically depends on both the central concentration of the systems and on the number of particles used to model them. For instance, halos of hosts and satellites at “ $z=0$ ” and “ $z=1$ ” always lie below the Dehnen model because they are more centrally concentrated (even more so when the adiabatic contraction is taken into account). On the other hand, the separation in the r_6 -coordinate between the optimal softening of the halos of hosts and satellites reflects the difference in the number of particles used to model them. In this sense it is easy to associate systems with a larger number of particles to smaller mean distances between particles and viceversa, given that the systems are compared in a normalised scale.

Also note that the disk satellite requires a halo that is better resolved at “ $z=1$ ” than for a spherical satellite in order to reach the best stability. This can be explained by the fact that a better resolved centrally concentrated region of the halo is able to inhibit the formation of non-axisymmetries (e.g., see Athanassoula et al. 2005).

2.4.3 Timestep

The timestep Δt has been defined for our simulations according to the standard criterion of Gadget-2.0. This means that the timestep for each particle is calculated as $\Delta t = \sqrt{2\eta\epsilon/|\mathbf{a}|}$, where η is a dimensionless parameter controlling the accuracy of the timestep criterion, ϵ is the softening associated to each particle, and \mathbf{a} is the gravitational acceleration suffered by each particle. Δt is also limited by a maximum value in order to prevent particles having too large timesteps. The maximum timestep is defined as a few percent of the timescale $t_c = 2\pi\epsilon/V_c(\epsilon)$ calculated for the component that has the smallest ϵ in the system, where V_c is the circular velocity. This ensures us that we follow the evolution of even the smallest components in the system with enough time resolution. We have set $\eta = 0.025$ and the maximum timestep to 0.25 Myr, which give us typical conservations of energy and angular momentum that are better than 0.1% over 9 Gyr of evolution for our main disk galaxy configured at “ $z=0$ ”.

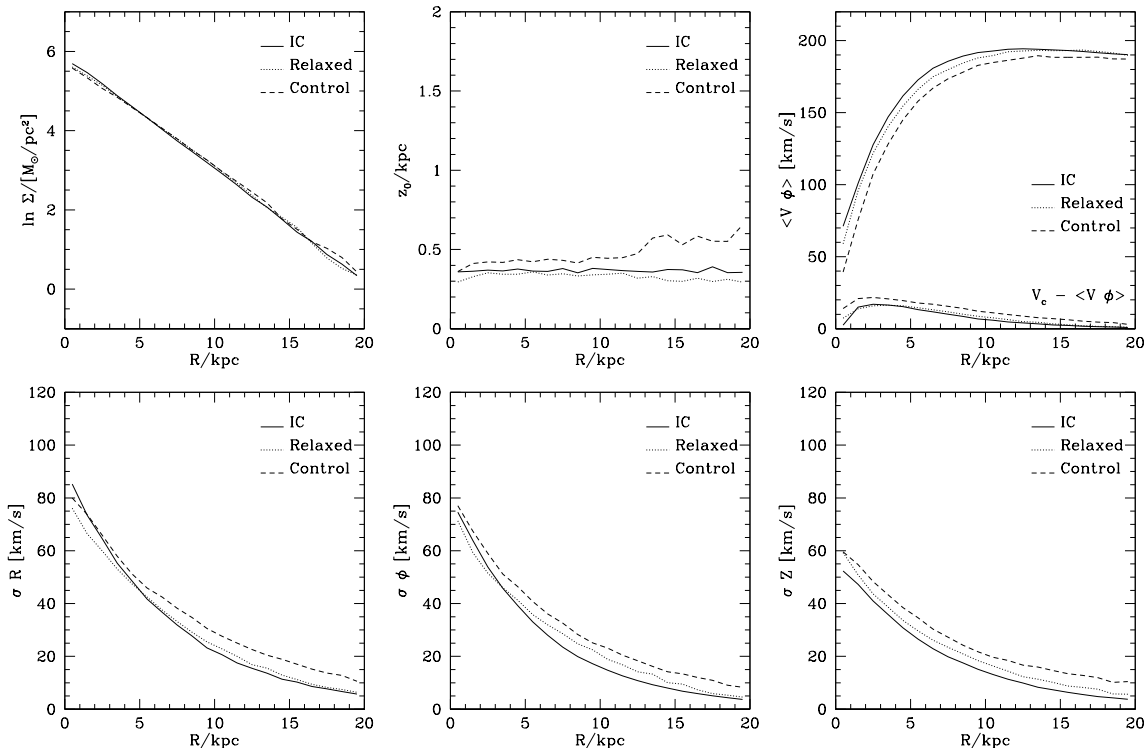


Figure 2. Evolution of the structural and kinematic properties of the isolated host disk, for the “ $z=0$ ” configuration. The solid lines show the initial conditions. The dotted lines show the disk after 1 Gyr of evolution within the fixed halo potential. The dashed lines show the disk’s evolution after 5 Gyr within the N -body halo. The latter model is used as the control case in the comparison to the minor merger simulations. A similar behaviour is obtained for the disk in the “ $z=1$ ” configuration.

2.5 Evolution of Isolated Host Galaxy

Before including the satellite, the host galaxy is simulated in isolation to test its stability in the absence of any external perturbation.

We first relax the disk component within a “rigid version” of the halo potential (which mimics the N -body halo described in §2.1.1) for a few rotational periods (normally 1 Gyr). Once the disk component is relaxed (i.e., there are no further changes in either its morphological or kinematical properties) the “rigid” halo is simply replaced by its N -body (“live”) counterpart, and evolved for additional 5 Gyr in isolation for the configuration at “ $z=0$ ”, and during 4 Gyr for that at “ $z=1$ ”. As described in §3.1, this time windows are enough to study the merger events that are of interest to us. Strong bar instabilities appear in the host galaxies evolved in isolation only after 9 Gyr and 7 Gyr for the configurations at “ $z=0$ ” and “ $z=1$ ”, respectively.

Fig. 2 shows how the initial properties of the host disk at “ $z=0$ ” change after being relaxed within a fixed halo for 1 Gyr, and after 5 Gyr in the live halo. Its properties are measured in concentric rings of 1 kpc of width, and including particles out to ~ 15 initial scale-heights. The surface density profiles $\Sigma(R)$ (top left panel) indicate that the scale-lengths of the disks (given by the inverse of the slope in log-linear scale) stay practically unchanged. Similarly, the vertical structure of the disk does not show significant evolution (top middle panel), except a moderate amount of flaring in the outer disk, presumably due to distant encounters be-

tween disk and halo particles. The scale-heights, measured at $R = 2.4R_D$, change from $z_0 = 0.35$ kpc to 0.41 kpc in the “ $z=0$ ” configuration and from 0.17 kpc to 0.24 kpc in the “ $z=1$ ” one. The disks are also slightly slowed down (top right), while the velocity dispersions show an increase of ~ 5 km/s in the first Gyr in the fixed halo, and a total of < 10 km/s after 6 Gyr of evolution in the live potential (bottom panels). The velocity ellipsoid of the disk (also measured at $R = 2.4R_D$) increases from $(\sigma_R, \sigma_\phi, \sigma_z) = (28, 20, 17.5)$ km/s to $(35, 28, 24)$ km/s in the “ $z=0$ ” configuration and from $(25, 18, 14)$ km/s to $(32, 28, 22)$ km/s in the “ $z=1$ ” one.

In summary, the procedure followed to generate the initial conditions and the criteria applied to define the values of the numerical parameters produce host galaxies that are very stable in their properties (cf., VW99; Font et al. 2001; Ardi et al. 2003; Gauthier et al. 2006; Hayashi & Chiba 2006) for the amount of time needed to complete the experiments. Therefore, we are now ready to focus on how these systems evolve when they suffer a minor merger.

3 RESULTS

In total, 25 simulations have been carried out to study the formation and global properties of thick disks as a result of the merger between a host disk galaxy and a satellite. The simulations explore combinations of the following elements: two configurations for the progenitors (“ $z=0$ ” and “ $z=1$ ”); two morphologies for the stellar component of the

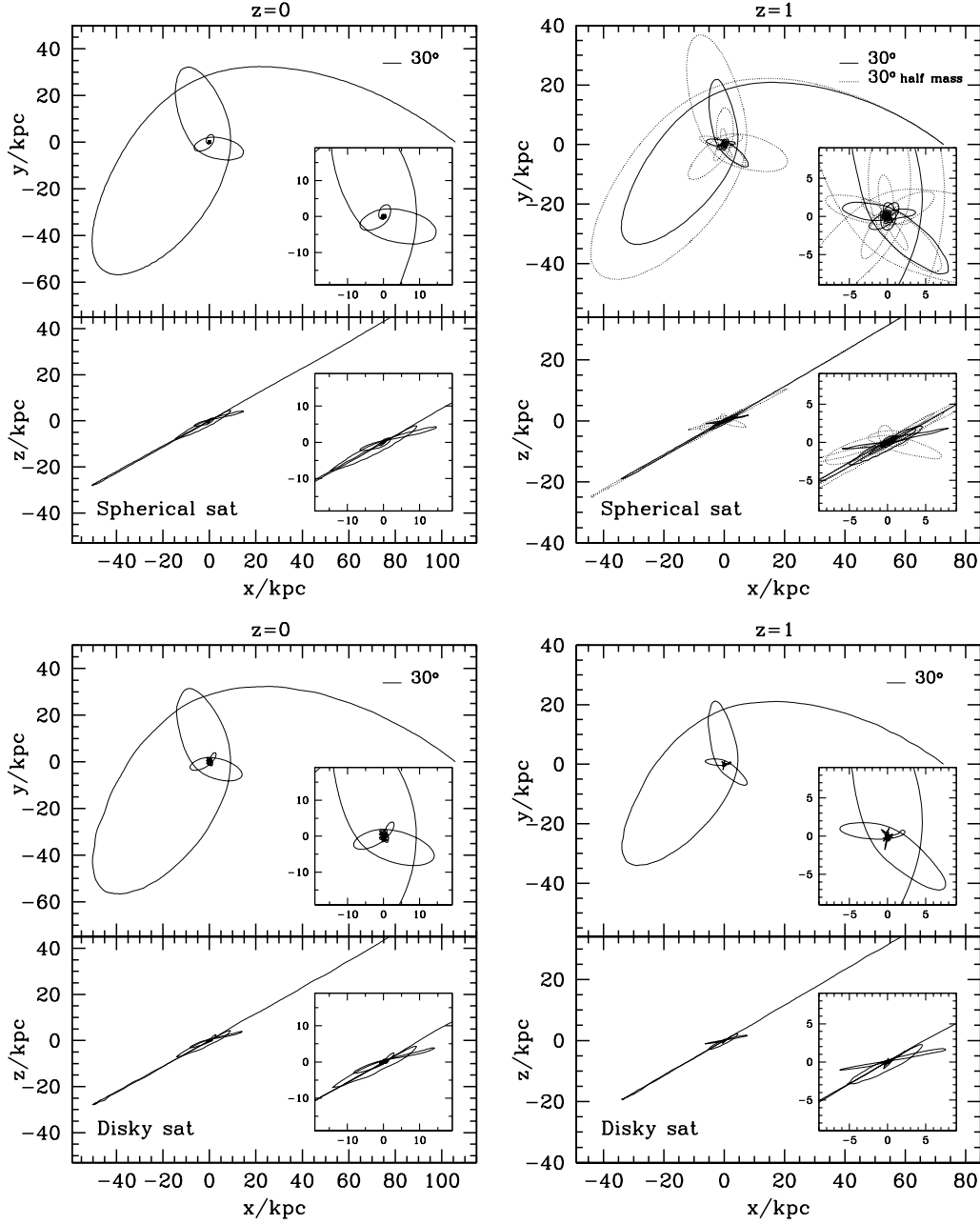


Figure 3. These figures show the orbital decay of the satellites. The panels show XY and XZ projections of the trajectory of the centre of mass of spherical and disk satellites as they decay towards the centre of the host galaxy in our “ $z=0$ ” and “ $z=1$ ” experiments. Each panel is centred on the host disk. The inset panels show in more detail the trajectory of the satellites in the final snapshots before they become fully disrupted.

satellite (spherical and disk); two total mass ratios between the satellite and the host galaxy (10% and 20%); and three initial orbital inclinations for the satellite with respect to the midplane of the host disk (0° , 30° and 60°), in both prograde and retrograde directions.

3.1 Orbital Evolution of the Satellites

To study the evolution of the orbits in our experiments we follow the location of the centre of mass of the satellite (CM)

with respect to the host galaxy. The CM is defined as the mean position of bound stellar and DM particles of the satellite. Fig. 3 shows the trajectories of the CMs for the experiments configured at “ $z=0$ ” and “ $z=1$ ” with spherical and disk (heavy and light) satellites in prograde orbits with initial inclination $i = 30^\circ$. The XY projections clearly illustrate how radial the orbits are and how rapidly they decrease in amplitude due to dynamical friction between the satellite and the host system. Note that these orbits are quite different from the circular ones usually used in earlier studies

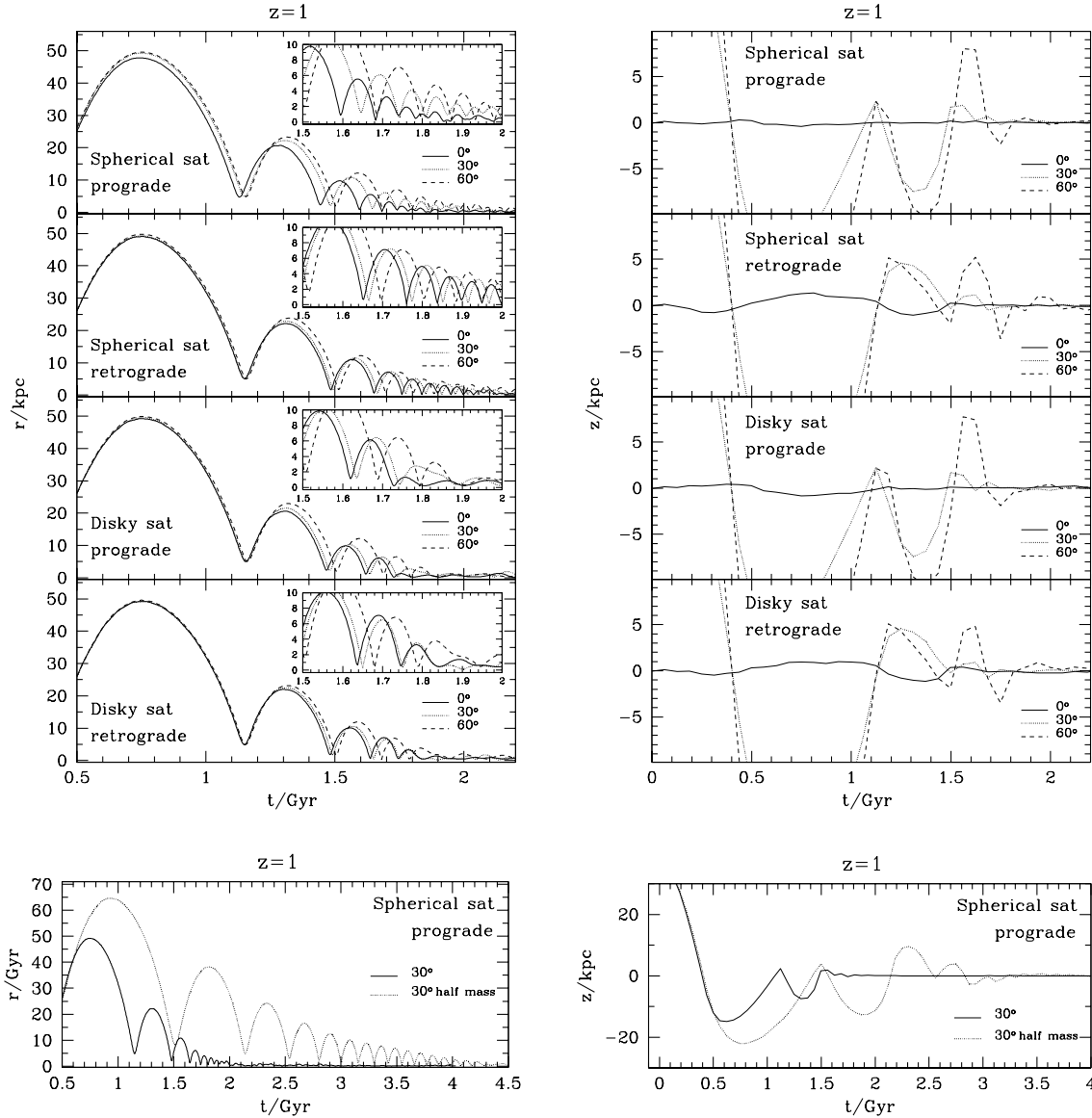


Figure 4. *Left:* Evolution of the separation between the centres of mass of the host disk and the satellite for different orbital inclinations and satellite morphologies for the “ $z=1$ ” configuration (a similar behaviour is observable for the “ $z=0$ ” case). *Right:* Evolution of the z -distance of the satellite’s centre of mass with respect to the host disk plane. The insets show in more detail the trajectory of the satellites at late times. The lack of a clear trend in the amplitude of the vertical oscillations seen in these panels is likely due to the difficulty in determining the exact orientation of the disk plane at the ~ 1 kpc level. The bottom panels show a comparison between the 10% and 20% spherical satellites for the inclination of 30° in the “ $z=1$ ” case.

(e.g., QG86; QHF93; WMH96). The YZ projections show that the satellites stay on their original orbital planes as they decay, until they enter into the zone dominated by the host disk, when they are drawn onto the disk plane and spiral in towards its centre. This is particularly clear for the lighter satellite in our “ $z=1$ ” experiment (see bottom right panel of Fig. 4) that spends ~ 1 Gyr on the disk plane before sinking in further.

Note that most of the angular momentum of the “satellite + host system” is in the orbital motion of the satellites. This is because the satellites are relatively massive and have a very large initial distance from the host. As a result, when

the satellite decays in an inclined orbit the disk is strongly tilted in both the prograde and retrograde cases (see §3.3).

As expected, the trajectory of the lighter satellite is more extended because the dynamical friction is less efficient in this case (Binney & Tremaine 1987). Our 20% satellites decay completely after ~ 3 Gyr in the case of “ $z=0$ ” experiments, and after ~ 2 Gyr for “ $z=1$ ” experiments. In comparison, the satellite with half of the mass takes the double of time to sink starting from the same initial orbital parameters, as shown in Fig. 4.

Initially, the orbital decay is due to the dynamical friction against the host halo. This implies that the decay rate does not depend on inclination, orbital direction or stellar

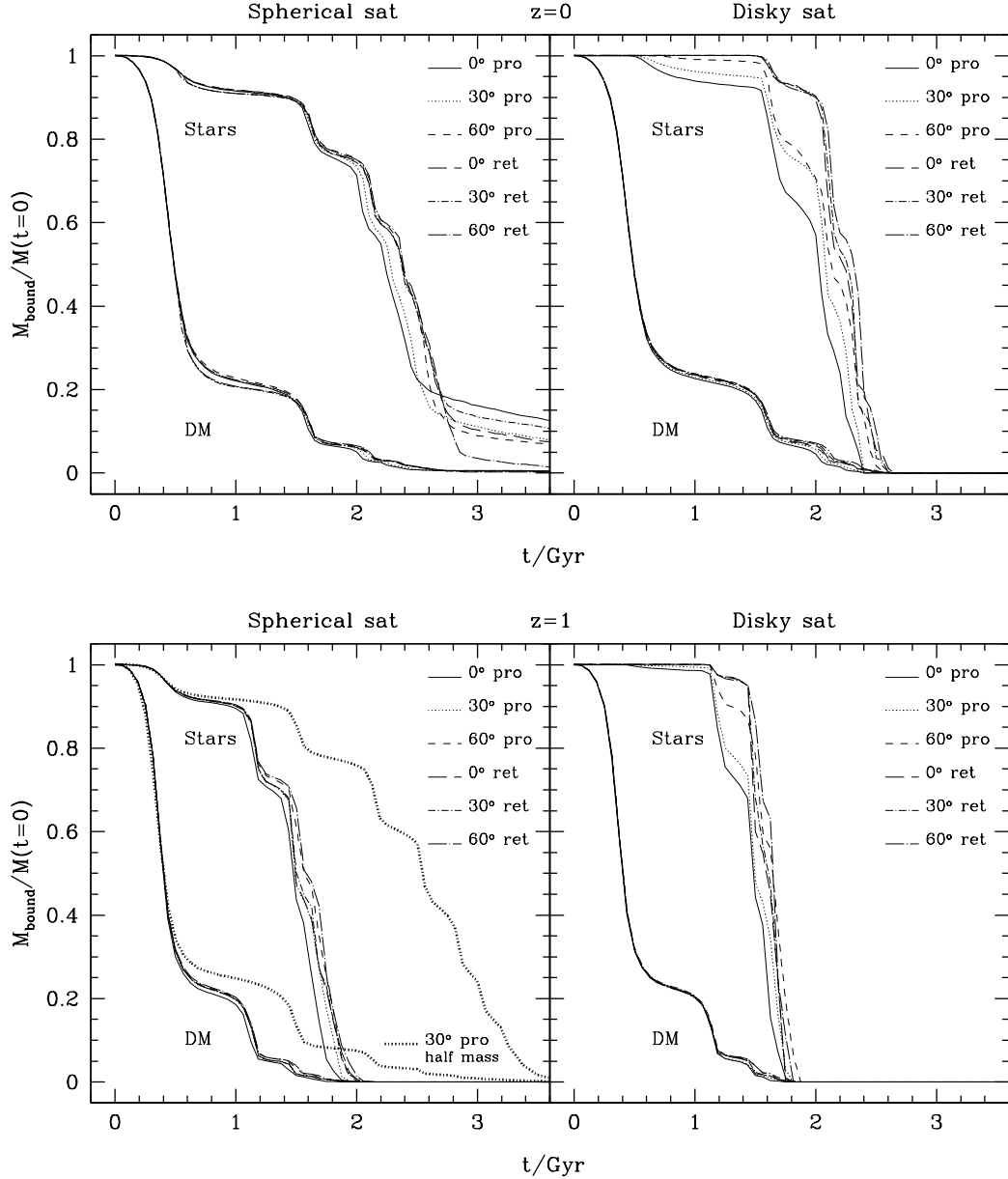


Figure 5. Mass that remains bound for both the dark matter and stellar components of the satellites in our experiments at “ $z=0$ ” (upper panels) and at “ $z=1$ ” (bottom panels). The bound mass is in units of the initial mass of the corresponding component.

mass distribution (see Fig. 4). On the other hand, when the satellites approach the centre of the system (where the disk is a significant contributor to the global force field), the orbit decays by dynamical friction also against the host disk. Thus at later times, prograde low inclination orbits decay faster than retrograde or high inclination orbits (QG86; WMH96; see also HC97).

3.2 Satellite Mass Loss

Fig. 5 shows the mass loss evolution of both DM and stellar components of spherical and disk satellites in the “ $z=0$ ” and “ $z=1$ ” experiments.

In order to calculate how much mass remains bound to

the satellite at a given time we implemented in Gadget-2.0 the following procedure (Benson et al. 2004):

- (i) Start by considering all the satellite particles that were bound to the satellite at the previous timestep (or simply all satellite particles for the first timestep).
- (ii) Compute the mass of the satellite from these particles along with the position and velocity of the CM.
- (iii) For each particle in this set, determine whether it is gravitationally bound to the other particles in the set.
- (iv) Retain only those particles that are bound and go back to step (ii). Repeat until the mass of the satellite has converged.

Since the satellites were initialised in the absence of an

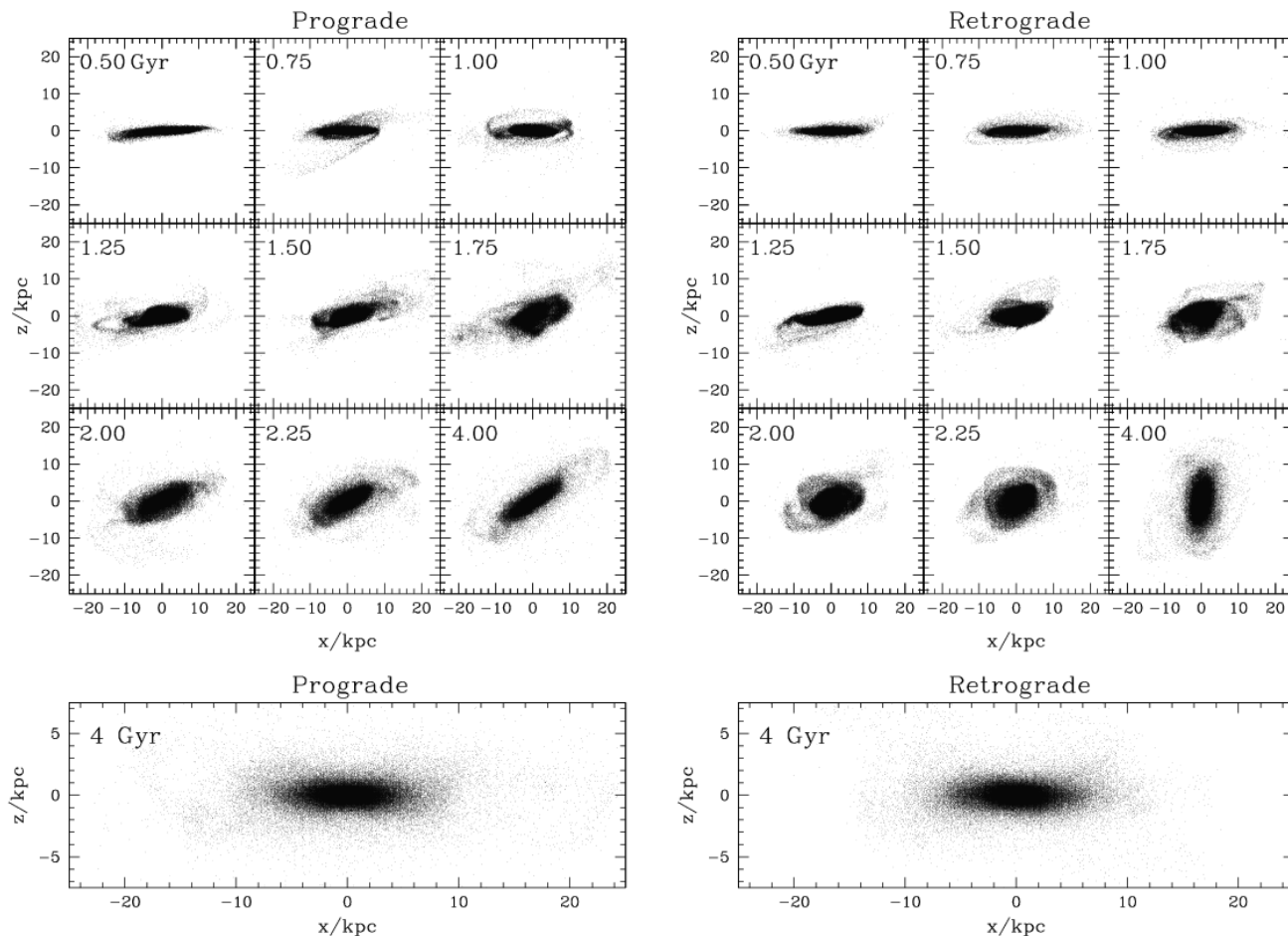


Figure 6. Evolution of the host disk (initially shown edge-on) during the merger with a spherical satellite with inclination of 30° for prograde and retrograde orbits in the “ $z=1$ ” experiment. Only host disk particles are shown for clarity. Note that the disk appears overthickened or distorted because of projection effects, especially in the case of the retrograde orbit. The bottom panels show edge-on views of the final disk.

external potential, as soon as they are placed within the host potential a large fraction (70%) of the more extended DM component rapidly becomes unbound before the first pericentric passage. After that, the mass loss rate of the DM component mostly depends on its initial mass.

The mass loss rate of the stellar components depend strongly on initial mass, and orbital parameters (WMH96; HC97; VW99) but also on the stellar mass distribution. As satellites decay, prograde orbits with lower inclinations lose mass faster than retrograde orbits with higher inclinations, due to the stronger tidal interaction with the host galaxy. This trend is more notorious for disk satellites. Spherical satellites are also characterised by a more extended “knee” in the mass loss in comparison to disk satellites. The lighter satellite experiences a slower mass loss compared to heavier satellites, because it suffers less dynamical friction and hence is on a less bound orbit.

Once a satellite has sunk onto the plane of the host disk, its fate will depend on its instantaneous mean density compared to the mean density of the host at the given location. If the mean density of the satellite is larger than that of the host system then the most bound particles of the satellite will reach the galactic centre as a distinctive

core causing more damage to the host disk. Otherwise, the satellite will receive most of the damage, being heated and torn apart by the host disk. In our simulations only the mergers with spherical satellites in the “ $z=0$ ” experiments deposit in the galactic centre final cores of up to 20% the initial stellar mass. These final cores are on the lighter side in comparison with previous studies defining high density satellites (QHF93, 20%; WMH96, 45%). It is interesting to note that spherical satellites with higher inclinations give rise to the formation of less massive cores. This can be explained by the fact that satellites on higher inclinations experience more disk crossings through the host disk as they decay, compared to ones on lower inclinations. In this case disk shocks perturb the structure of the satellite and cause additional mass loss (see Binney & Tremaine 1987; QHF93).

3.3 Description of the Mergers

Figs. 6, 7 and 8 illustrate the morphological changes in the thick disk progenitors during the merger event when they are configured at “ $z=1$ ”, and when the initial inclination of each satellite is 30° for both prograde and retrograde cases.

As the satellite decays in its orbit, it induces the for-

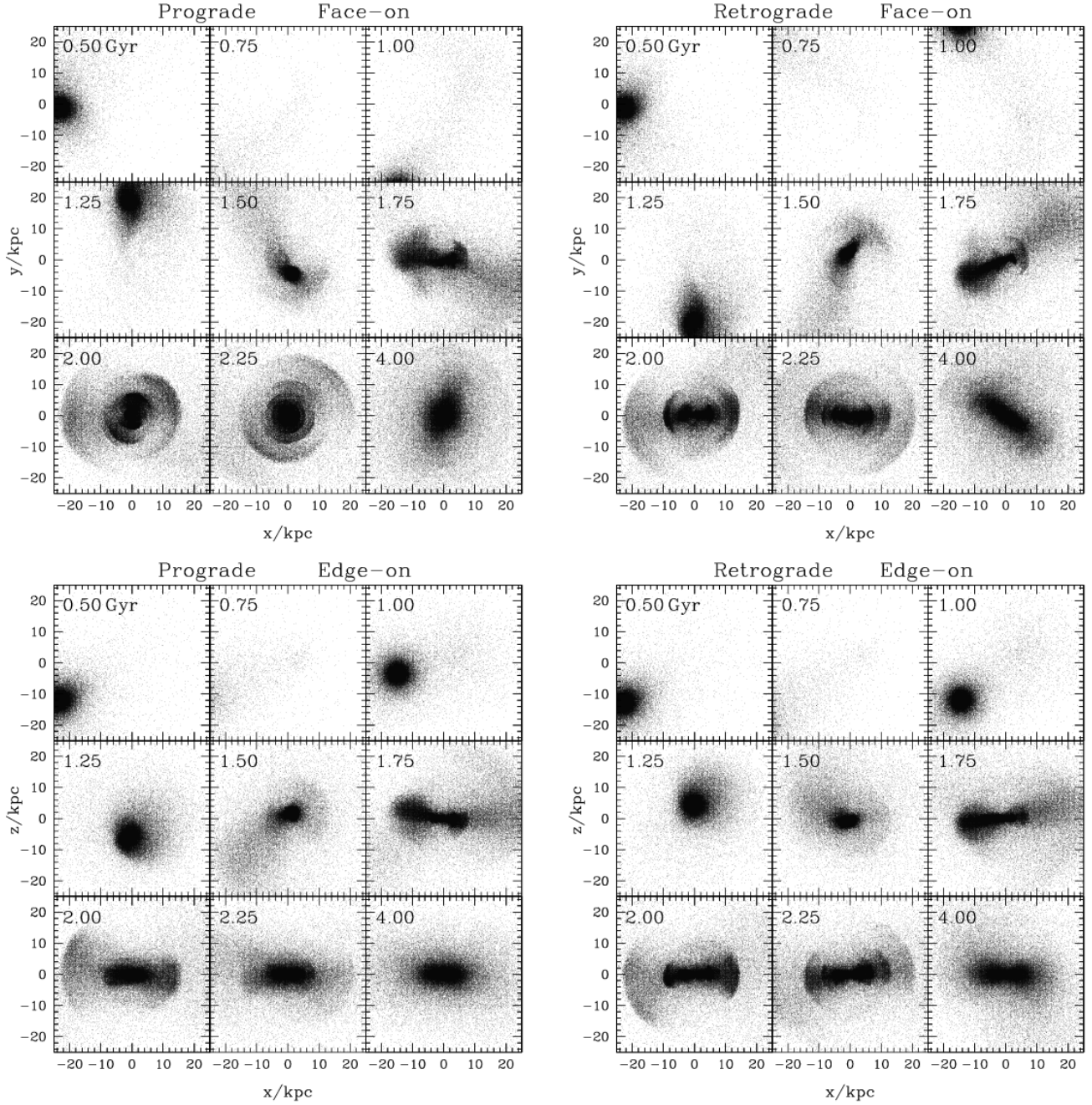


Figure 7. Evolution of the spherical satellite with inclination 30° during the merger with the host galaxy in the “ $z=1$ ” experiment. In each snapshot the reference frame has been centred on the centre of mass of the host disk and has also been rotated to eliminate the tilting of the whole system with respect to the original frame. The labels *face-on* and *edge-on* are relative to the host disk (not shown here for clarity).

mation of noticeable spiral arms in the host disk (Fig. 6), which transport angular momentum from the central parts towards the outskirts (QHF93). Once the satellite sinks onto the plane of the host disk it transfers kinetic energy from its orbit to the particles in the disk, increasing their vertical motions and causing a visible thickening. At the same time the disk responds to the decaying satellite, by tilting its plane in order to conserve the total angular momentum of the system (QHF93) (although a significant amount of

the satellite’s initial angular momentum has by this time, already been transferred to the host halo).

The top panels of Figs. 7 and 8 show the distribution of star particles in a face-on view with respect to the instantaneous disk orientation, while the bottom panels corresponds to the edge-on view. In the early stages of the orbital decay, the satellite is stripped leaving trails of particles on orbits with inclinations similar to that of the satellite initially. Since the stars are initially deeply embedded in the satellite’s

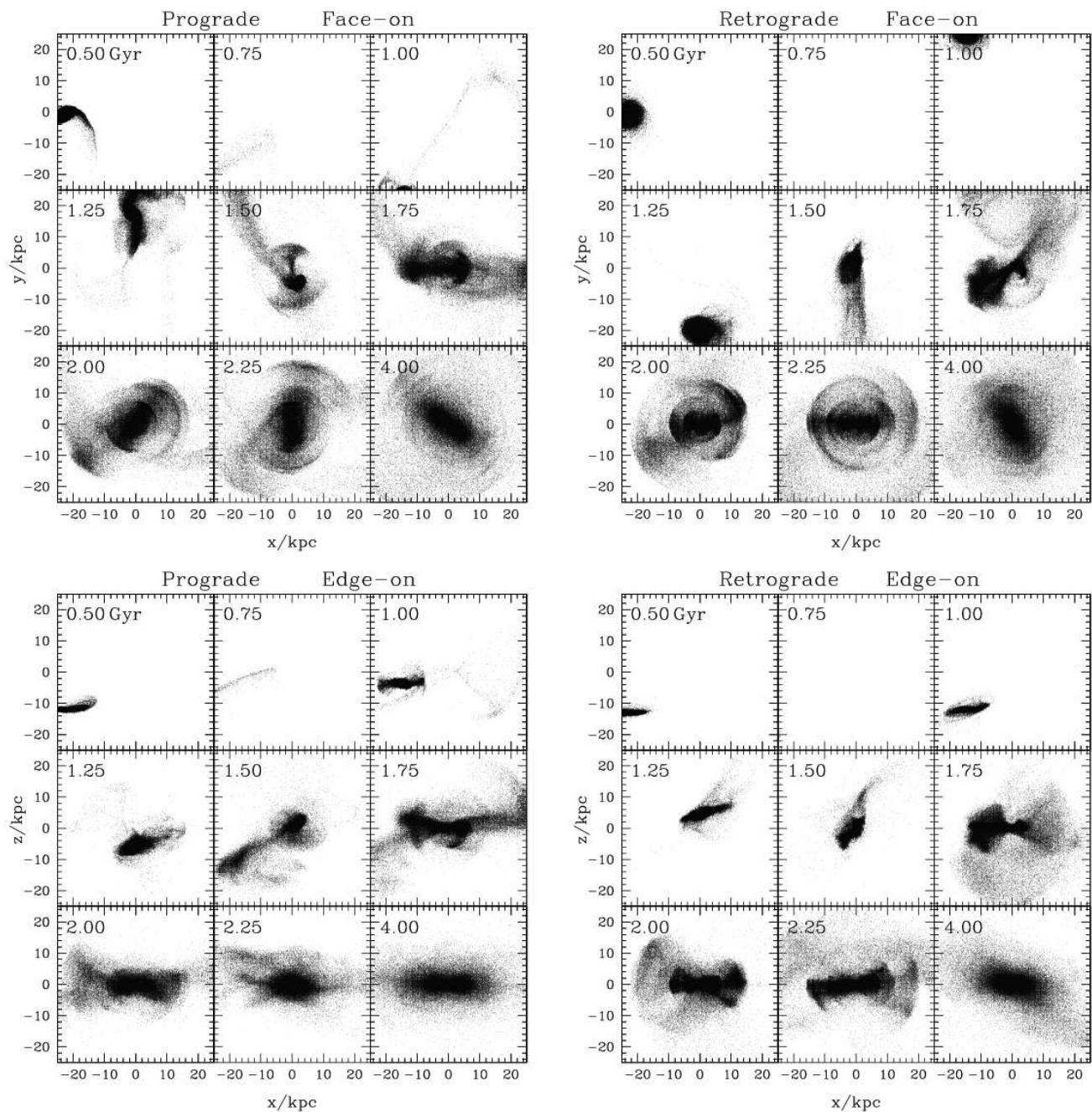


Figure 8. Same as Fig. 7, for the case of the disk satellite.

dark matter halo, only a small fraction of the stellar debris is deposited at large radii. Most of the stars from the satellite end up in a disk-like configuration, with the same orientation as the final disk, but one that is somewhat thicker and more extended (see §3.4). Noticeable shells of debris material are formed as time goes by. These structures are a consequence of the interaction of a dynamically cold system with a larger one (Hernquist & Quinn 1988). In general the survival of these shells will depend on the mean phase-space density of the infalling satellite and also on its orbit. In the case of spherical satellites shells are visible typically since $t \sim 1.7$ Gyr, lasting ~ 2 Gyr; and for disk satellites

much sharper shells are seen starting at $t \sim 1.5$ Gyr, being still noticeable by the end of the simulation, i.e., ~ 2.5 Gyr later. Shells are rather common features related to merger events, being observed in many elliptical and spiral galaxies (Schweizer 1980; Malin & Carter 1983; Sadler & Gerhard 1985; Schweizer & Seitzer 1988; Wilkinson et al. 2000). An important characteristic of shells is that they usually survive for a long time in physical space, as previous numerical studies have shown (Quinn 1984; Dupraz & Combes 1986; Hernquist & Quinn 1988, 1989; Heisler & White 1990). The presence of such a structures in the solar vicinity and the possible signatures imprinted on them during the formation

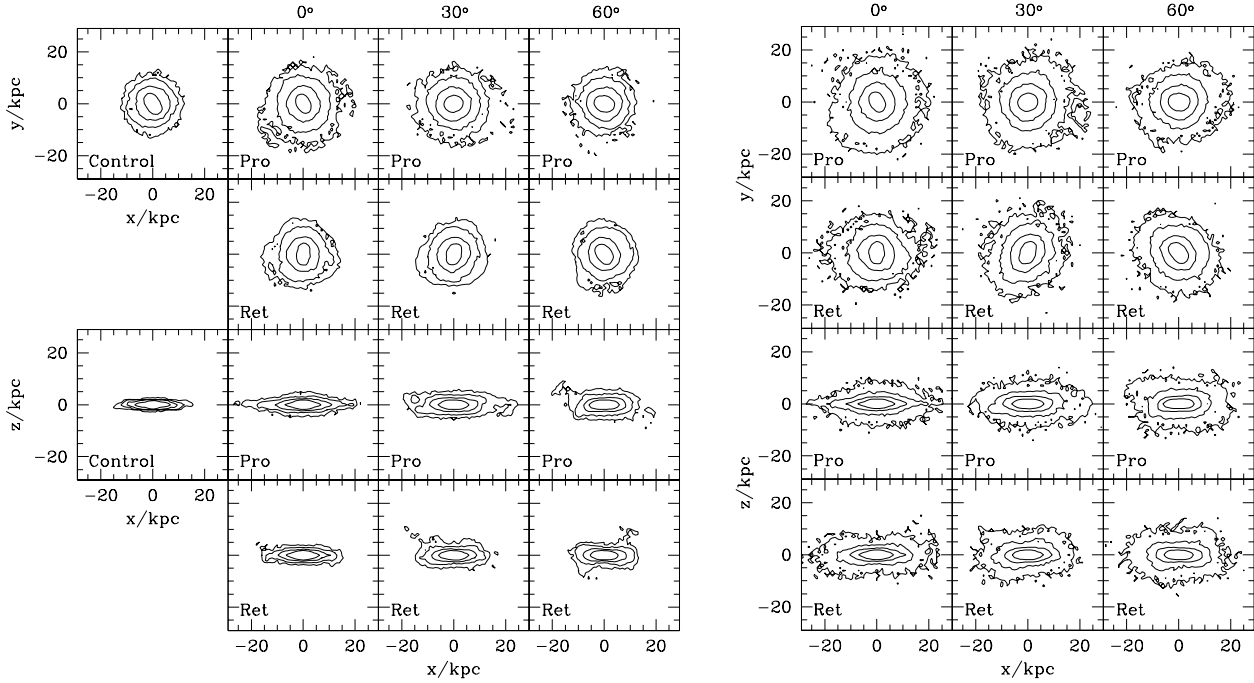


Figure 9. Face-on and edge-on views of the final morphologies of heated disks (left) and thick disks (right) at the end of the simulations in “ $z=1$ ” experiments; 4 Gyr after the infall of the spherical satellite. In each case the tilting induced by the satellites has been eliminated to facilitate the comparison with the coeval control disk. The contours correspond to 22.5 mag/arcsec² (innermost), 24.2 mag/arcsec², 26 mag/arcsec² and 27.7 mag/arcsec² (outermost) in the V-band, after assuming a mass-to-light ratio $\Upsilon_V = 2\Upsilon_{\odot,V}$.

of the thick disk will be explored in Paper II (note that such features have already been proposed to explain the Monoceros ring, see e.g. Helmi et al. 2003).

By the end of the simulations both the morphological and kinematical properties of the heated disks and satellite debris have settled and do not evolve further. This occurs ~ 2 Gyr after either the satellite has been disrupted or its core has reached the centre of the host disk. This means that the properties of the final thick disks do not change after $t=5$ Gyr and $t=4$ Gyr for the systems configured at “ $z=0$ ” and at “ $z=1$ ” respectively, in the case of heavy satellites. This timescale is ~ 6 Gyr for the lighter satellite in our “ $z=1$ ” experiment.

The left panels in Fig. 9 show the morphologies of the heated host disks at the final time of the “ $z=1$ ” experiments, for the case of the spherical satellites. Prograde orbits and lower inclinations induce on the host moderate arms and more radial expansion in comparison with retrograde orbits and higher inclinations. On the other hand, higher prograde inclinations are more efficient at thickening the disk, especially at the outskirts. For instance, a prograde satellite with inclination of 60° only causes a slight increment of the radial extension compared to the coeval control disk, but induces a noticeable thickening compared to the same control disk and to the other inclinations. Satellites on retrograde orbits have a similar thickening effect on the disk but a considerably milder influence on the formation of tidal arms and radial expansion compared to satellites on prograde orbits. Notice also that the satellites during their decay induce the formation of weak bars. Some warping in the disks is also

visible in the case of mergers with inclinations of 60° for both prograde and retrograde orbits (see QHF93; VW99).

The panels on the right side of Fig. 9 show the thick disks obtained, now including the contribution of the satellite’s stellar particles. Their final structure is dominated by the heated disk (compare to the left panels), except in the outer regions, where the contribution of satellite debris is important. The outskirts are clearly thicker for satellites on higher inclination orbits, although their debris does not show the warp feature characteristic of the heated disks. Also noticeable is the difference in the distribution of satellite debris between prograde and retrograde orbits for the case of coplanar infall (in edge-on views). Overall, the morphologies of the thick disks closely resemble the structures of real edge-on galaxies that show the presence of thick disks (e.g., see Dalcanton & Bernstein 2000).

The contour levels shown in this figure have been drawn at 22.5 mag/arcsec², 24.2 mag/arcsec², 26 mag/arcsec² and the outermost contour is at 27.7 mag/arcsec² in the V-band, after assuming a mass-to-light ratio $\Upsilon_V = 2\Upsilon_{\odot,V}$ both for the disk as well as for the satellite stars. The outermost contours are at surface brightness levels comparable to those reached by e.g., Dalcanton & Bernstein (2000, 2002). This implies that the change in the shape of the surface brightness contours from the centre to the outskirts as well as the irregularity of the outermost contours could be detectable with current instrumentation. Note that the boxy nature of the outermost contours could in principle be used as a strong discriminant for the formation of thick disks via mergers.

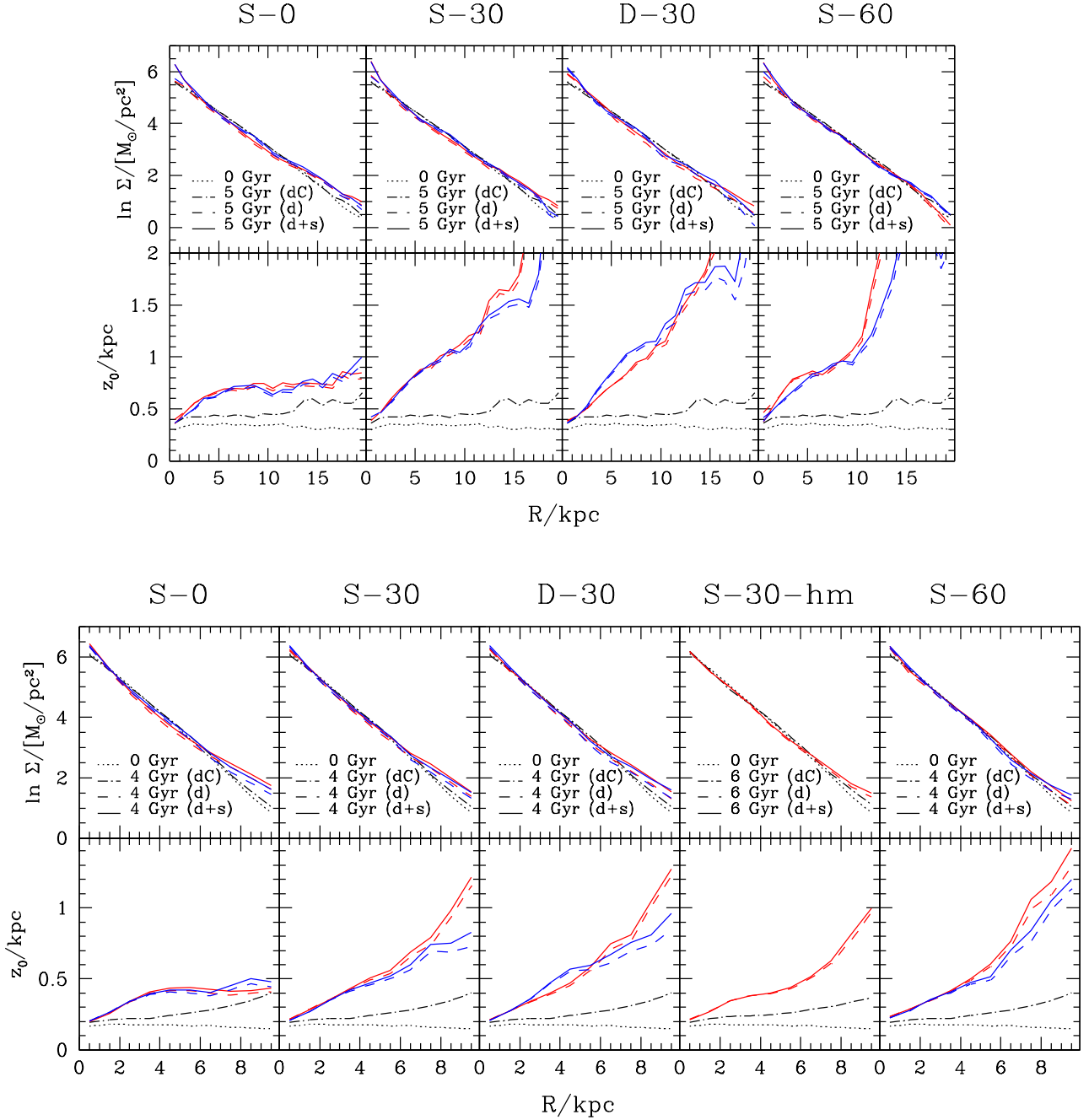


Figure 10. Final structural properties of thick disks for our “ $z=0$ ” (top) and “ $z=1$ ” (bottom) experiments, as a function of radius for different satellite morphologies and orbital inclinations. The column “hm” corresponds to the lighter satellite (with half the mass). Red and blue lines correspond to prograde and retrograde orbits, respectively. The properties have been measured using only “star” particles from the disk (dashed) or disk and satellite (solid). As reference, the initial (dotted) and final state (dashed-dotted) of the disk in the control model is included.

3.4 Properties of the Thick Disks

We now study in more detail the morphological and kinematical properties of the final thick disks. To this end we use a reference frame centred on the centre of mass of the final product, and aligned with its principal axes in such a way that the rotation axis defines the z -direction.

The properties of the thick disk are computed in con-

centric rings, and hence are azimuthally averaged, as described in §2.5. This implies that non-axisymmetric features such as bars and warps are not subtracted before the analysis is made. All the properties have been computed taking into account star particles from both the pre-existing (heated) disk and the satellite. Their relative contribution has been appropriately weighted according to the initial

$M_{\text{sat},\text{stars}}/M_{\text{host,disk}}$ ratio to account for the fact that the satellite particles have smaller masses.

3.4.1 Structural Properties

Fig. 10 shows the surface mass densities and scale-heights of the simulated thick disks as a function of radius. The top panels correspond to the “ $z=0$ ” configurations while those in the bottom to the “ $z=1$ ” ones. Each panel is for a different inclination or different type of satellite (spherical, disky or half-mass) on prograde (red) and retrograde orbits (blue). The properties of the control disk galaxy are also shown at the initial (dotted curves) and final times (dash-dotted curves) to calibrate the effect of the mergers against the intrinsic evolution of the host. In order to estimate the contribution of the satellite particles on the final thick disk, the properties of the heated host disks are plotted separately (dashed curves).

For both “ $z=0$ ” and “ $z=1$ ” experiments, the surface density profiles show a mild dependence on orbital inclination, having slightly higher surface brightness in the outskirts for lower inclinations. This tendency is mostly due to the host disk material that is transported radially outwards during the merger by transfer of energy and angular momentum. Even though the variation is small amongst the various experiments, it is enough to produce larger scale-lengths in the thick disks (compared to the control disk) for lower satellite inclinations as we will see below (see also Fig. 9). As expected, the lighter spherical satellite (in the “ $z=1$ ” experiment) produces a smaller variation in the surface density at larger radius. In general the contribution of satellite particles to the spatial structure of final thick disks is very small. This is true at all radii except at the centre where the very dense spherical satellites accreted in the “ $z=0$ ” experiment are not completely disrupted, retaining a core and giving rise to a small “bulge-like” component (see also Fig. 5). The surface density profile does not show any strong dependence on orbit direction.

The final vertical density profiles resemble the shape of the initial distribution of the disk $\rho_d(z) = \rho_0 \text{sech}^2(z/2z_0)$ albeit with different scale-heights. As shown in Fig. 10 the scale-heights increase with radius (flaring), indicating that both heated disk and satellite particles at larger galactic radii are orbiting at larger distances from the midplane. Flared disks like those in our simulations have already been observed in previous studies (e.g. QG86), suggesting that flaring is a rather generic characteristic of disks heated by mergers (see Kazantzidis et al. 2007, for a derivation of how the scale-height varies with radius due to minor mergers).

The final scale-heights also depend strongly on the initial inclination of the satellite’s orbit being largest for highly inclined orbits. The disks thicken more when merging with satellites on higher inclinations because of the significantly large vertical kinetic energy associated to the satellites’ orbital motion which is transferred to the disk. Spherical and disky satellite do not induce very different vertical heating on the disks. Note that less massive satellites produce final thick disks that are thinner.

Fig. 11 shows the final scale-lengths of the thick disks as a function of the initial orbital inclinations of the satellites. This figure quantifies what is observed qualitatively in Fig. 9 and also from the surface density profiles (Fig.

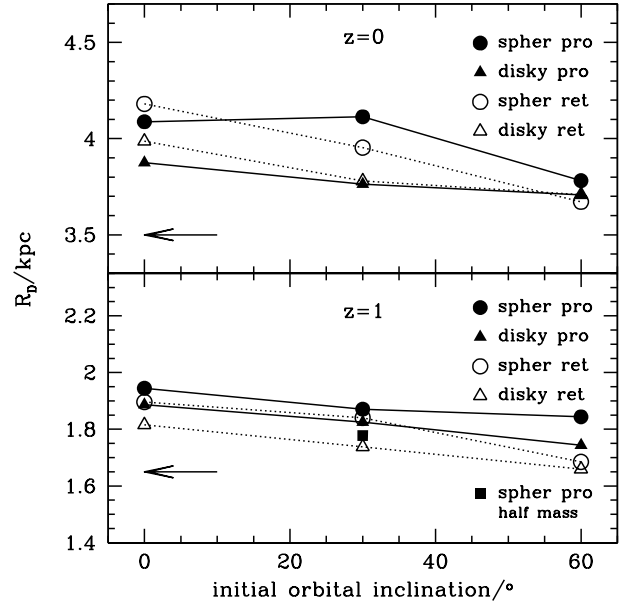


Figure 11. Scale-lengths of the final thick disks as a function of initial orbital inclination of the satellites for the “ $z=0$ ” and “ $z=1$ ” experiments. As reference, the arrows show the initial scale-length of the host disks.

10). As expected, the satellites with the lowest inclinations induce the largest changes in the scale-lengths. This is because the orbital energy of the satellite is essentially deposited mostly into radial motions of the stars in the disk for a low inclination encounter. The lighter satellite causes a smaller increment in the scale-lengths than heavier satellites. This is because a lighter satellite transfers less energy and angular momentum to the host disk as it decays, producing less extended both heated and thick disks. We also find that prograde orbits are slightly more efficient in inducing an increase in the scale-length of the disk. This increase in the scale-length appears to be consistent with observations which suggest that thick disks tend to have larger scale-lengths than thin disks (e.g., Yoachim & Dalcanton 2006).

In Fig. 12 we plot the final relative number $N_s/(N_s + N_d)$ of stellar satellite particles as a function of radius in the resulting thick disks for mergers configured at “ $z=0$ ” and “ $z=1$ ”. Recall that the number of satellite particles has been renormalised according to $N_s = N_{\text{sat},\text{stars}} \times M_{\text{sat},\text{stars}}/M_{\text{disk}}$.

As mentioned before, in the “ $z=0$ ” experiments, spherical satellites have a higher mean density than the host disk. This causes the core to reach the host disk centre almost intact, representing $\sim 50\%$ of the total number of particles near the centre of the final thick disk. In comparison, this ratio drops to 5% for the disky satellites. At both intermediate and larger radii the fraction of particles from the spherical satellites is roughly constant, independently of either orbital inclination or sense of rotation. On the other hand disky satellites are disrupted at large radii, where their debris is deposited. Furthermore, the lower the inclination, the higher the fraction at a given radius, as naturally expected.

For the “ $z=1$ ” both spherical and disky satellites are

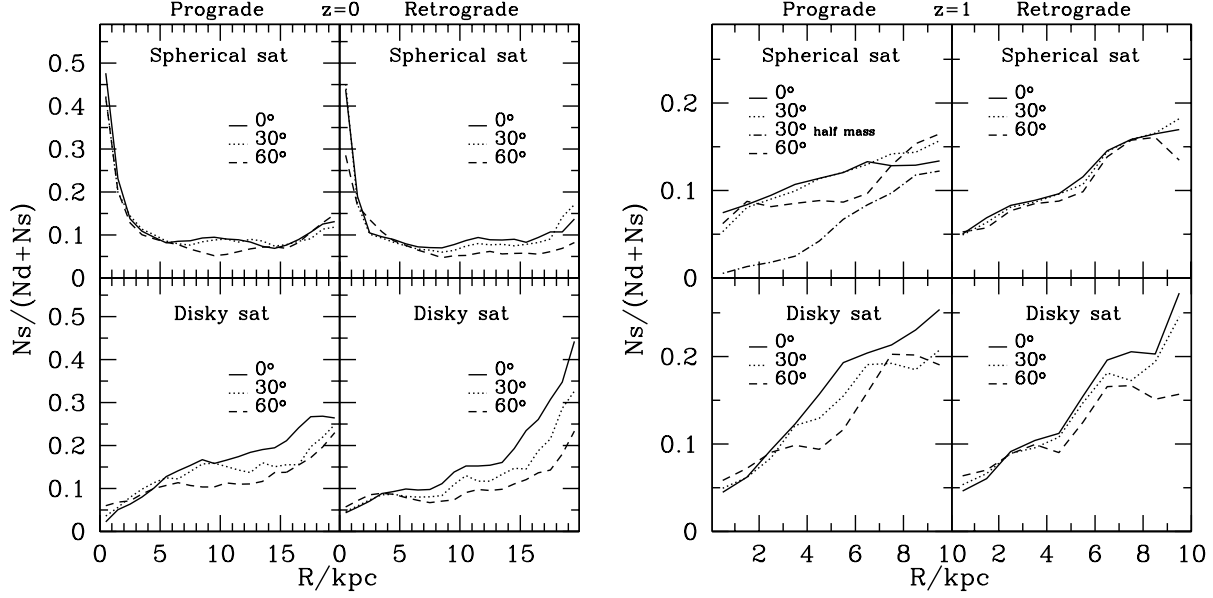


Figure 12. Relative number of satellite particles in the final thick disks as a function of cylindrical radius for the “ $z=0$ ” (top) and “ $z=1$ ” (bottom) experiments.

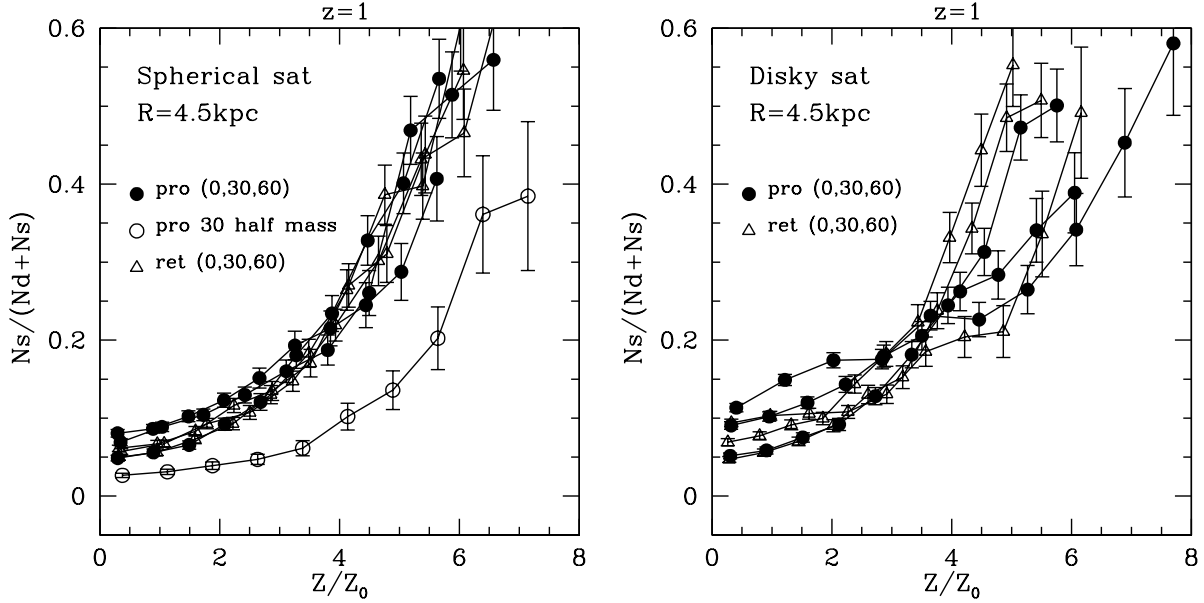


Figure 13. Relative number of satellite particles in the final thick disks for our “ $z=1$ ” experiments, as a function of distance from the disk plane. Distances from the plane are normalised by the respective scale-height at a distance of $R = 4.5$ kpc, which corresponds to 2.4 scale-lengths of the original disk.

completely destroyed. The relative fraction of satellite stars increases with radius and, as expected, at the centre the relative number of satellite particles is smaller for the lighter satellite. The observed trend with orbital inclination in spherical and disk satellites at “ $z=0$ ” is confirmed for the “ $z=1$ ” configuration.

Fig. 13 shows the fraction of satellite particles plotted now as a function of the vertical direction at a radius $R=4.5$ kpc, for spherical and disk satellites in the “ $z=1$ ” experiments. The radius corresponds to 2.4 initial scale-lengths in

this experiment. This figure shows that the fraction of accreted particles as a function of distance from the plane, when normalised by the respective scale-height, *only* depends on the mass ratio between the satellite and host. E.g., at $z = 4z_0$ the fraction of particles reflects the mass ratio of the merger. The same behaviour is observed in the “ $z=0$ ” experiments.

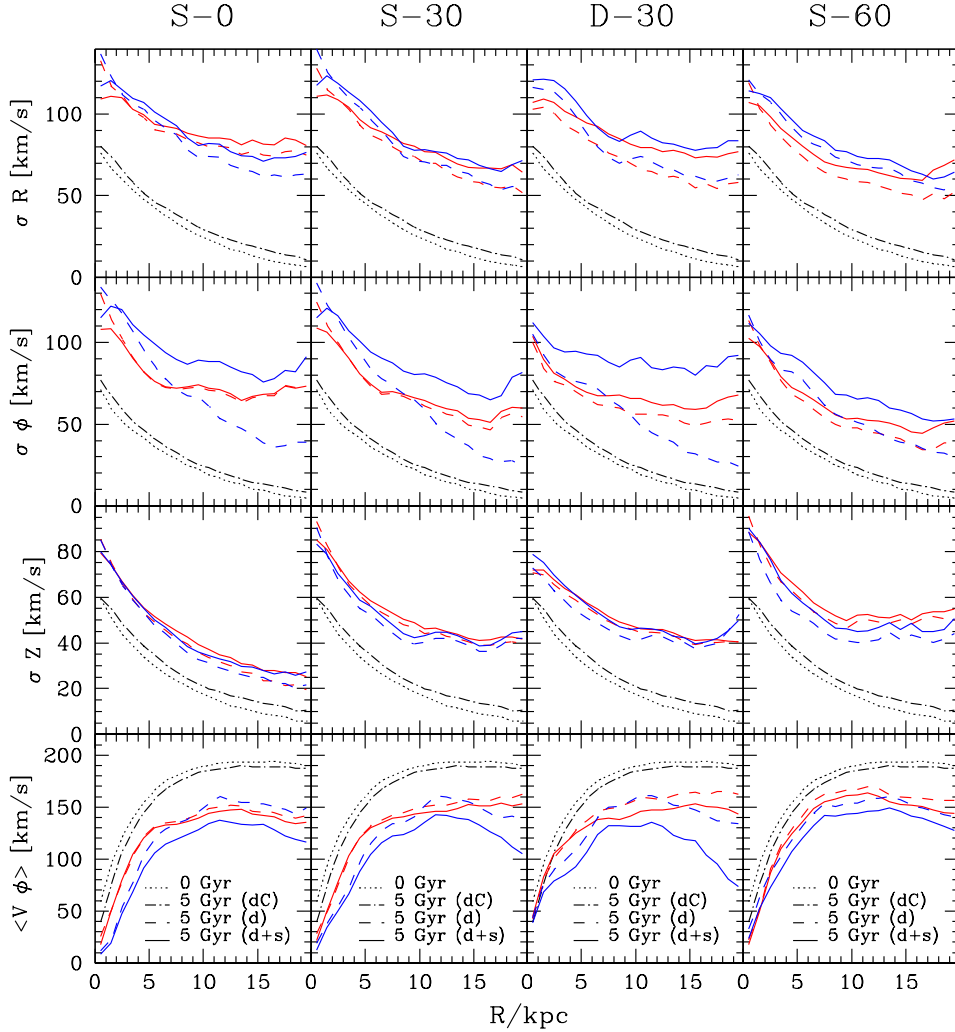


Figure 14. Final dynamical properties of thick disks for our “ $z=0$ ” experiments, as a function of radius for different satellite morphologies and orbital inclinations. Red and blue lines correspond to prograde and retrograde orbits, respectively. The properties have been measured using only “star” particles from the disk (dashed) or disk and satellite (solid) located within 5 kpc from the disk plane. As reference, the initial (dotted) and final state (dashed-dotted) of the disk in the control model is included.

3.4.2 Kinematical Properties

The transformation of orbital energy into thermal energy (random motions) in the disk is evident in Figs. 14 and 15. Here we show the radial, azimuthal and vertical velocity dispersions along with the mean rotational velocities in thick disks as a function of radius for the various simulations in our “ $z=0$ ” and “ $z=1$ ” experiments. These quantities have been computed in volumes centred on the plane whose thickness in the z -direction is a fixed fraction of the initial scale-height of the disk. For the “ $z=0$ ” experiments it corresponds to 5 kpc, while it is ~ 3 kpc for the “ $z=1$ ” ones.

The velocity dispersions in the plane of the disk (σ_R and σ_ϕ) are larger for lower inclination orbits. The opposite trend is observed for the vertical velocity dispersion σ_Z . This is not surprising given our previous discussion on the evolution of the scale-heights and scale-lengths and their dependence on orbital inclination.

Satellites on retrograde orbits appear to have only a

slightly lower efficiency in transferring their orbital energy to heating the disk in the vertical direction than their prograde counterparts. There are no clear trends with respect to orbital sense for the radial direction (σ_R) for the heated disk stars. On the other hand, the azimuthal velocity dispersions of the heated disk stars (dashed in Figs. 14 and 15) are significantly smaller at large radii for retrograde orbits, except for those with high inclination. However, one should bear in mind that observationally we will generally not be able to distinguish the (light of the) stars from the heated disk and from the satellite. This means that one would measure the global σ_ϕ , i.e., the solid curve in the bottom panels of Figs. 14 and 15, which is, of course, significantly larger for retrograde experiments.

In general, mean rotational velocities $\overline{v_\phi}$ of thick disks differ noticeably from the coeval control simulation in all cases, by dropping ~ 60 km/s although with a mild dependence on the orbital inclination. Low inclination encounters produce thick disks that rotate slower, implying larger asym-

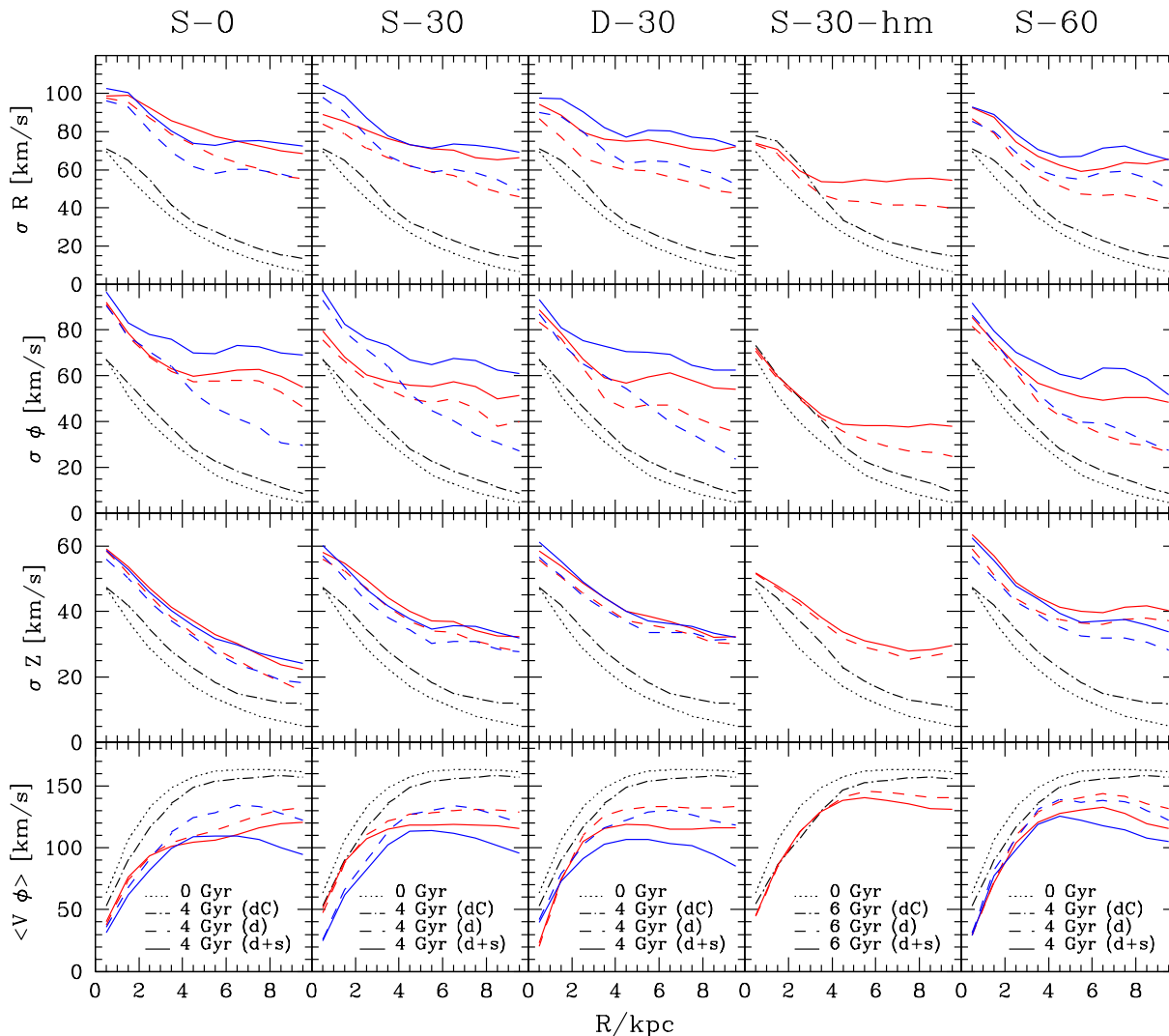


Figure 15. Final dynamical properties of thick disks for our “ $z=1$ ” experiments, as a function of radius for different satellite morphologies and orbital inclinations. The column “hm” show the satellite with half the mass. Red and blue lines correspond to prograde and retrograde orbits, respectively. The properties have been measured using only “star” particles from the disk (dashed) or disk and satellite (solid) located within 3 kpc from the disk plane. As reference, the initial (dotted) and final state (dashed-dotted) of the disk in the control model is included.

metric drifts. This is also evidenced by their larger radial and azimuthal velocity dispersions, as discussed above. As expected, the mean rotational velocity of thick disks which are the result of encounters with satellites on counter-rotating orbits, is lower due to the contribution of the accreted stars. This difference is more evident at larger radii, where the satellite stars are found in larger numbers (see Fig. 12), but is never greater than 10-20 km/s near the outer edge of the disk compared to the peak value.

The mean rotational velocity also shows noticeable differences with inclination when it is measured away from the midplane of the thick disk (Fig. 16). Satellites with lower initial orbital inclinations induce a rotational lag, whose magnitude increases with height above the plane. This is because such satellites are more efficient in heating the disk radially at every height, leading to a larger asymmetric drift.

In Fig. 17 we have plotted the ratio σ_Z/σ_R as a function

of radius for the different experiments. The original and the control disk show a constant $\sigma_Z/\sigma_R \sim 0.7$ value and no trend with radius. This figure clearly shows that σ_Z/σ_R can be used to make a clear discrimination of the initial inclination of the satellite. The reason for this strong dependence on inclination is essentially due the fact that a satellite on a highly inclined orbit will induce a much larger change in σ_Z at large radii than a satellite on a co-planar orbit.

4 DISCUSSION

Previous works investigating the response of a host disk galaxy to one or more infalling satellites provide us with a valuable description of the dynamical effects involved in the process (QG86; Tóth & Ostriker 1992; QHF93; WMH96; HC97; VW99; Benson et al. 2004). HC97 find that a massive

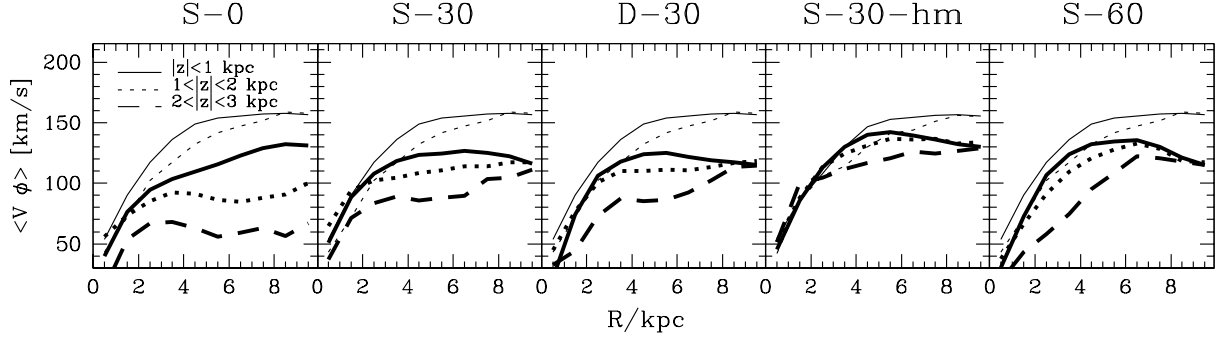


Figure 16. Mean azimuthal velocities of thick disk “stars” at several heights above the plane as a function of radius for our “ $z=1$ ” experiments in prograde orbits. Thick lines include particles from both the heated disk and satellite, while the thin lines correspond to the disk in the control model (the highest z -range is not shown in this case because there are too few disk particles at that distance from the midplane). The same behaviour is observed in our “ $z=0$ ” experiments.

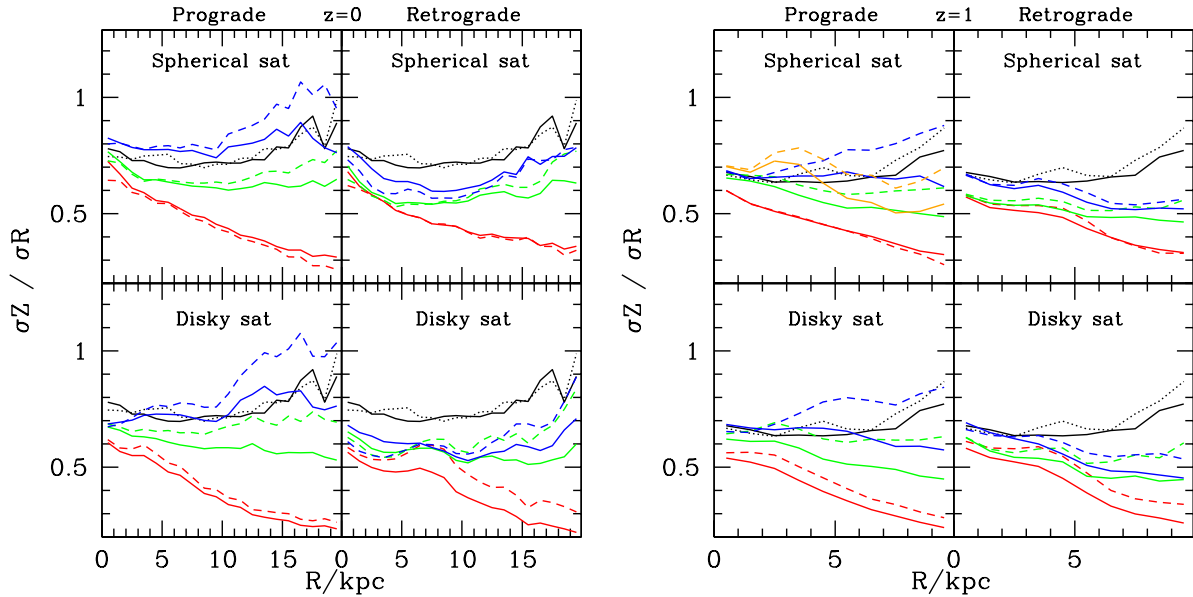


Figure 17. Final σ_z/σ_R as a function of distance on the plane for different initial stellar distributions and orbital inclinations of the satellites: 0° (red), 30° (green) and 60° (blue). Dashed lines refer to disk-only and solid to disk+satellite. The control disk has a constant $\sigma_z/\sigma_R \sim 0.7$ at both the initial (black dotted) and final (black solid) time.

satellite (30% of M_{disk}), as it decays due to dynamical friction, can tilt the orientation of the disk up to 10° and cause warping. These effects illustrate the strong transfer of angular momentum from the infalling satellite to the host disk. VW99 note that satellites in prograde orbits mostly increase the disk heating. On the other hand retrograde orbits are more efficient in tilting the disk orientation. Benson et al. (2004) show that more massive and more concentrated satellites increase the difference between the amount of disk heating caused by prograde and retrograde orbits. QG86 indicate that most of the kinetic energy of the infalling satellite is deposited on the plane of the disk and a small quantity heats up the vertical motions of disk particles. This shows that velocity dispersions in the host disk are not increased isotrop-

ically by the satellite. QHF93 note that most of the heating on the plane of the disk is caused by spiral arms stimulated by the decaying satellite. These arms also transfer angular momentum radially outwards, expanding the disk. QG86 and QHF93 also show that the vertical structure of the disk is not uniform across the disk. Instead, the scale-height of the host disks increases at larger radii. Our simulations are able to confirm most of the aforementioned dynamical effects and also show a significantly larger tilting than previously found, both for the prograde and retrograde cases. This can be traced back to the fact that in our experiments, the accreted satellite is initially much more massive and is launched from a significantly larger distance (see §3.3).

4.1 Choice of massive satellites to heat disks up

Cosmological simulations show that massive mergers like those in our “ $z=1$ ” experiments are likely to have happened during the life-time of a Milky Way-sized host system. For instance, Kazantzidis et al. (2007) estimate the number of massive subhalos accreted since $z \sim 1$ as at least one object with a mass $\sim M_{\text{disk}}$ and five objects more massive than $20\% M_{\text{disk}}$. This is consistent with other simulations like GA3n (Stoehr 2003), whose merger tree reveals that at least one subhalo with a mass of the order of $2 \times 10^{11} M_{\odot}$ is accreted by $z \sim 1$. Even though massive mergers may be less frequent they are able to reach the centre of the host system thanks to dynamical friction, causing important changes in the structure and kinematics of the host disk. In principle, this could imply that a Milky Way-like disk would experience only one severe change of orientation since $z \sim 1$ and also that only one massive satellite would be needed to heat up a pre-existing disk to give rise to a thick disk.

4.2 Observations of thick disks

Pohlen et al. (2004) have carried out photometric thick/thin disk decompositions and characterised properties such as scale-length and scale-height for a sample of eight S0 edge-on galaxies by fitting 3D disk models. The authors find that the mean scale-height of the thick disk is between 2.4 and 5.3 times larger than that of the thin disk; while the mean scale-length is about twice, ranging from 1.6 to 2.6. In general these values confirm the results obtained by other authors for S0, Sab, Sb, Sbc, Scd and Sd galaxies (e.g., van der Kruit 1984; de Grijs & van der Kruit 1996; de Grijs & Peletier 1997; Pohlen et al. 2004; Yoachim & Dalcanton 2006), including the Milky Way (Ojha 2001; Larsen & Humphreys 2003). If we assume that the structure of a thick disk is not strongly affected by the formation of a new thin disk, and that our initial “thin” disks may represent present-day systems, we can take the scale-heights obtained for our experiments at the final time at face value and compare them to the initial configuration. Typically there is an increase in the scale-height by a factor 2 – 3.6, while the scale-lengths are only slightly larger (with final-to-initial ratios between 1 and 1.2). These values appear to be in agreement with the range of ratios observed in general in spiral galaxies.

Kinematically, the values of the velocity ellipsoids of our thick disks, measured at $R \approx 2.4R_D$, are in good agreement with the one observed at the solar radius in the Milky Way ($(\sigma_R, \sigma_\phi, \sigma_z) \sim (65, 54, 38)$ km/s (e.g., see Layden et al. 1996; Chiba & Beers 2001; Soubiran et al. 2003; Alcobé & Cubarsi 2005; Soubiran & Girard 2005; Vallenari et al. 2006). The values of σ_z/σ_R measured by these authors are typically ~ 0.6 , suggesting that the thick disk of the Galaxy could have been produced by a merger of intermediate inclination (see Fig. 17). The differences between the mean rotational velocity of the final thick disk and that of the pre-existing disk are $\Delta \overline{v}_\phi \sim 40\text{--}50$ km/s. Note that these values cannot be interpreted directly as the observed rotational lag between the thin and thick disks in the Milky Way since we do not include gas in our simulations that later on can collapse and actually form a new thin disk (see §4.4.1).

4.3 Our simulations in the context of M31

It is important to notice that in our experiments configured at “ $z=0$ ” the initial properties of the host disk, before the merger with the satellite, resemble the properties of the current thin disk of the Galaxy. This implies that the final thick disks generated in our experiments are too massive and do not represent direct analogues of the thick disk of the Milky Way. However this set of simulations may be useful in understanding the evolution of M31, which is likely to have experienced recent merger events as may be inferred from the rich and complex structures present in its outskirts (Ibata et al. 2007, and references therein).

For example, Ibata et al. (2005) discovered an extended and clumpy disk-like structure around M31 with a scale-length similar to that of the main disk, rotating ~ 40 km/s slower and with a rather low velocity dispersion of ~ 30 km/s. Its stellar population has homogeneous kinematics and abundances over the entire region where it is observed, which suggests that it was formed in a single global event. However, it is not straightforward to link the extended disk of M31 to the thick disk modeled here, mainly because of the much higher velocity dispersions of the final thick disks in our simulations.

The giant stream of M31 (Ibata et al. 2001, 2004), thought to originate in the disruption of a satellite with mass $\sim 10^9 M_{\odot}$, and the so-called eastern and western “shells” (Ferguson et al. 2002; Irwin et al. 2005; Ibata et al. 2007), may be related given the similarities of their stellar populations. In the context of our simulations, this would be quite natural. Analogous structures are observed as the satellite is disrupted as shown in Figs. 7 and 8 for prograde orbits in face-on view at 1.5 Gyr (see also Fardal et al. 2007; Mori & Rich 2008). It is interesting to note that much sharper and longer lasting shells are generated by disk satellites compared to spherical ones.

4.4 Caveats

4.4.1 Lack of gas physics in our simulations

In this paper we have focused on the collisionless interactions between a disk galaxy and a satellite, with both dark matter and stellar components, without including gas physics nor star formation which may affect the interactions and the final thick disk’s properties. This is potentially the most crucial simplifying assumption in this study, and one that needs to be addressed in future work, since disk galaxies were presumably much more gas rich at high redshift (Robertson et al. 2006).

The lack of gas physics implies that the modeled disks do not grow in stellar mass or in size during the timespan of the merger (except of course through the dynamical heating processes described above). Furthermore, it is likely that such mergers would likely trigger a (strong) burst of star formation. These new stars would be relatively old and located in a thinner structure. On the other hand, some orbital energy deposited by the infalling satellite into the gas could be radiated away from the system, reducing the dynamical damage done to the disk (QHF93). The remaining (and presumably heated) gas would eventually cool and settle down to form a new thin disk. This slow accumulation of gas on the midplane should induce a contraction of the thick disk.

For example, Elmegreen & Elmegreen (2006) estimate that this contraction leads to a decrease in the scale-height of the contracted thick by $\sim 40\%$ and an increase of the velocity dispersion by $\sim 50\%$.

4.4.2 Time-dependance of gravitational potential

In general, the structure of a dark matter halo evolves with time through mergers and slow accretion. However, in our simulations we have neglected any cosmological evolution of the structure of the host halo during and after the merger with the satellite. This simplification may be justified by recent studies (e.g., Wechsler et al. 2002; Zhao et al. 2003; Romano-Díaz et al. 2006; Diemand et al. 2007), which have shown that the structure of dark halos is very stable within the scale radius r_s after the phase of active mergers, which for a disk galaxy must have ended at redshifts $\sim 0.5 - 1$. This is indeed the region that we follow dynamically in our simulations, after the initial decay of the satellite due to dynamical friction, which lasts typically less than 1 Gyr. Therefore, the final thick disks are well within this scale radius, being $r_s \sim 6$ and ~ 11 times the final scale-lengths in the “z=0” and “z=1” experiments, respectively.

5 SUMMARY AND CONCLUSIONS

We have performed numerical simulations of the heating of a disk galaxy by a single relatively massive merger. These mergers lead to the formation of thick disks whose characteristics are similar, both in morphology as in kinematics, to those observed in the Milky Way and other spiral galaxies.

The simulations explore several configurations of the progenitor systems whose properties have been scaled at two different redshifts in order to study the formation of thick disks at different epochs. The satellites have total masses of 10% and 20% that of the host galaxy and have been modeled as a stellar component immersed in a dark matter halo. The stellar components have either a spherical or disk distribution. The satellites have been released far away from the host disk, with initial orbital parameters that are consistent with cosmological studies. Additionally, three different initial orbital inclinations of the satellites have been studied in both prograde and retrograde directions with respect to the rotation of the host disk.

We find that as the satellite galaxies spiral in through dynamical friction, significant asymmetries are visible, both in the host disk and in the to satellite debris. Particularly interesting are the low surface brightness shells, especially visible in the outskirts of the final thick disks, that last for about 1.5 to 2 Gyr after the merger has been completed. These shells acquire relevance in the case of Andromeda where according to recent studies a couple of these features are likely associated to the event that also gave rise to the giant stream (Ibata et al. 2001, 2004; Ferguson et al. 2002, 2005; Fardal et al. 2007; Mori & Rich 2008).

Despite the relatively large mass ratios, the infalling satellites do not fully destroy the host disk, but merely heat it and tilt it. The host disks are found to change their orientation both for the prograde and retrograde encounters.

The scale-lengths of the final thick disks are slightly more extended than those of the original host disk while

the scale-heights are almost four times larger, depending on the initial inclination of the satellite. The scale-heights are not constant as a function of galactic radius, but show a noticeable flare. If this is the case for the thick disk of the Milky Way, part of the flared material could be (confused with) the Monoceros ring.

Interestingly, the fraction of satellite particles at a given galactic radius as a function of height above the plane, when normalised by the respective scale-height, *only* depends on the mass ratio between the satellite and host and not on stellar morphology of the satellite or type of orbit. For instance, at a distance of 4 scale-heights the fraction of satellite particles reflects the mass ratio of the merger.

We find that satellite stars do not dominate the luminosity until rather far above the midplane, which may suggest that it would be quite difficult to find counter-rotating disks produced by the mechanism studied here. In this sense, the possible existence of a counter-rotating thick disk, detected by Yoachim & Dalcanton (2005) only ~ 2 thick-disk scale-heights above the midplane, challenges the formation through a single minor merger onto a thin disk, favouring instead a scenario where the thick disk formed by direct accretion of stars from an infalling satellite. However, relatively fast rotating thick disks (like the one of the Milky Way) may be more easily explained by disk heating formation, since a random distribution of accreted satellites would have less chance of producing thick disks with strong coherent rotation.

Kinematically, the velocity ellipsoids of the simulated thick disks are in good agreement with observations of the Galactic thick disk at the solar radius. The rotational lag may also be consistent with observations, if we neglect further significant evolution due to the formation of a thin disk component from freshly accreted gas. The observed trend of the ratio σ_Z/σ_R with radius in the final thick disks is found to be a very good discriminant of the initial inclination of the decaying satellite. In the case of the Milky Way, the observed σ_Z/σ_R at the position of the Sun is ~ 0.6 (e.g., Chiba & Beers 2001; Vallenari et al. 2006), suggesting that the thick disk of the Galaxy could have been produced by a merger of intermediate inclination. Measurements of the mean rotational velocity in the final thick disks, at several heights from the midplane, indicate that satellites with lower initial inclinations are more efficient in introducing asymmetric drifts dependent on height. This implies that the possible existence of vertical gradients in the mean rotational velocity in the thick disk of the Galaxy (Girard et al. 2006) would also favour mergers with either low or intermediate orbital inclination.

In paper II we will explore in detail the phase-space structure of the merger product with the goal of constraining further the mechanism described here for the formation of the Galactic thick disk.

ACKNOWLEDGEMENTS

We thank M. C. Smith and L. Sales for stimulating discussions and suggestions. We thank S. C. Trager and R. Sanders for useful remarks. We acknowledge financial support from the Netherlands Organisation for Scientific Research (NWO). The simulations were run in the Linux clus-

ter at the Centre for High Performance Computing and Visualisation (HPC/V) of the University of Groningen in The Netherlands.

REFERENCES

- Abadi M. G., Navarro J. F., Steinmetz M., Eke V. R., 2003, *ApJ*, 597, 21
- Aguirri J. A. L., Balcells M., Peletier R. F., 2001, *A&A*, 367, 428
- Alcobé S., Cubarsi R., 2005, *A&A*, 442, 929
- Ardi E., Tsuchiya T., Burkert A., 2003, *ApJ*, 596, 204
- Athanassoula E., Fady E., Lambert J. C., Bosma A., 2000, *MNRAS*, 314, 475
- Athanassoula E., Lambert J. C., Dehnen W., 2005, *MNRAS*, 363, 496
- Bekki K., Chiba M., 2001, *ApJ*, 558, 666
- Benson A. J., 2005, *MNRAS*, 358, 551
- Benson A. J., Lacey C. G., Frenk C. S., Baugh C. M., Cole S., 2004, *MNRAS*, 351, 1215
- Binney J., Merrifield M., 1998, *Galactic astronomy*. Princeton, NJ, Princeton University Press, 1998, 850 p.
- Binney J., Tremaine S., 1987, *Galactic dynamics*. Princeton, NJ, Princeton University Press, 1987, 755 p.
- Blumenthal G. R., Faber S. M., Flores R., Primack J. R., 1986, *ApJ*, 301, 27
- Brook C. B., Gibson B. K., Martel H., Kawata D., 2005, *ApJ*, 630, 298
- Brook C. B., Kawata D., Gibson B. K., Freeman K. C., 2004, *ApJ*, 612, 894
- Bryan G. L., Norman M. L., 1998, *ApJ*, 495, 80
- Burkert A., Truran J. W., Hensler G., 1992, *ApJ*, 391, 651
- Burstein D., 1979, *ApJ*, 234, 829
- Chen B., Stoughton C., Smith J. A., Uomoto A., Pier J. R., Yanny B., Ivezić Ž., York D. G., Anderson J. E., Annis J., Brinkmann J., Csabai I., Fukugita M., Hindsley R., Lupton R., Munn J. A., the SDSS Collaboration 2001, *ApJ*, 553, 184
- Chiba M., Beers T. C., 2001, *ApJ*, 549, 325
- Dalcanton J. J., Bernstein R. A., 2000, *AJ*, 120, 203
- Dalcanton J. J., Bernstein R. A., 2002, *AJ*, 124, 1328
- de Grijs R., Peletier R. F., 1997, *A&A*, 320, L21
- de Grijs R., van der Kruit P. C., 1996, *A&AS*, 117, 19
- de Rijcke S., Michielsen D., Dejonghe H., Zeilinger W. W., Hau G. K. T., 2005, *A&A*, 438, 491
- Diemand J., Kuhlen M., Madau P., 2007, *ApJ*, 667, 859
- Dupraz C., Combes F., 1986, *A&A*, 166, 53
- Eddington A. S., 1916, *MNRAS*, 76, 572
- Eggen O. J., Lynden-Bell D., Sandage A. R., 1962, *ApJ*, 136, 748
- Eke V. R., Cole S., Frenk C. S., 1996, *MNRAS*, 282, 263
- Elmegreen B. G., Elmegreen D. M., 2006, *ApJ*, 650, 644
- Fardal M. A., Guhathakurta P., Babul A., McConnachie A. W., 2007, *MNRAS*, 380, 15
- Ferguson A. M. N., Irwin M. J., Ibata R. A., Lewis G. F., Tanvir N. R., 2002, *AJ*, 124, 1452
- Ferguson A. M. N., Johnson R. A., Faria D. C., Irwin M. J., Ibata R. A., Johnston K. V., Lewis G. F., Tanvir N. R., 2005, *ApJ*, 622, L109
- Font A. S., Navarro J. F., Stadel J., Quinn T., 2001, *ApJ*, 563, L1
- Freeman K., Bland-Hawthorn J., 2002, *ARA&A*, 40, 487
- Fuhrmann K., 2004, *Astron. Nachr.*, 325, 3
- Gauthier J.-R., Dubinski J., Widrow L. M., 2006, *ApJ*, 653, 1180
- Gilmore G., Reid N., 1983, *MNRAS*, 202, 1025
- Gilmore G., Wyse R. F. G., 1986, 322, 806
- Gilmore G., Wyse R. F. G., Norris J. E., 2002, *ApJ*, 574, L39
- Girard T. M., Korchagin V. I., Casetti-Dinescu D. I., van Altena W. F., López C. E., Monet D. G., 2006, 132, 1768
- Hayashi H., Chiba M., 2006, 58, 835
- Heisler J., White S. D. M., 1990, *MNRAS*, 243, 199
- Helmi A., Navarro J. F., Meza A., Steinmetz M., Eke V. R., 2003, *ApJ*, 592, L25
- Hernquist L., 1990, *ApJ*, 356, 359
- Hernquist L., 1993, *ApJS*, 86, 389
- Hernquist L., Quinn P. J., 1988, *ApJ*, 331, 682
- Hernquist L., Quinn P. J., 1989, *ApJ*, 342, 1
- Huang S., Carlberg R. G., 1997, *ApJ*, 480, 503
- Ibata R., Chapman S., Ferguson A. M. N., Irwin M., Lewis G., McConnachie A., 2004, *MNRAS*, 351, 117
- Ibata R., Chapman S., Ferguson A. M. N., Lewis G., Irwin M., Tanvir N., 2005, *ApJ*, 634, 287
- Ibata R., Irwin M., Lewis G., Ferguson A. M. N., Tanvir N., 2001, 412, 49
- Ibata R., Martin N. F., Irwin M., Chapman S., Ferguson A. M. N., Lewis G. F., McConnachie A. W., 2007, *ApJ*, 671, 1591
- Irwin M. J., Ferguson A. M. N., Ibata R. A., Lewis G. F., Tanvir N. R., 2005, *ApJ*, 628, L105
- Jensen E. B., Thuan T. X., 1982, *ApJS*, 50, 421
- Kazantzidis S., Bullock J. S., Zentner A. R., Kravtsov A. V., Moustakas L. A., 2007, *ArXiv:0708.1949*, 708
- Kazantzidis S., Magorrian J., Moore B., 2004, *ApJ*, 601, 37
- Khochfar S., Burkert A., 2006, *A&A*, 445, 403
- Kregel M., van der Kruit P. C., de Grijs R., 2002, *MNRAS*, 334, 646
- Kroupa P., 2002, *MNRAS*, 330, 707
- Larsen J. A., Humphreys R. M., 2003, *AJ*, 125, 1958
- Layden A. C., Hanson R. B., Hawley S. L., Klemola A. R., Hanley C. J., 1996, *AJ*, 112, 2110
- Lewis J. R., Freeman K. C., 1989, *AJ*, 97, 139
- Malin D. F., Carter D., 1983, *ApJ*, 274, 534
- Martin N. F., Ibata R. A., Bellazzini M., Irwin M. J., Lewis G. F., Dehnen W., 2004, *MNRAS*, 348, 12
- Mihos J. C., Walker I. R., Hernquist L., Mendes de Oliveira C., Bolte M., 1995, *ApJ*, 447, L87+
- Mo H. J., Mao S., White S. D. M., 1998, *MNRAS*, 295, 319
- Mori M., Rich R. M., 2008, *ApJ*, 674, L77
- Morrison H. L., Miller E. D., Harding P., Stinebring D. R., Boroson T. A., 1997, *AJ*, 113, 2061
- Mould J., 2005, *AJ*, 129, 698
- Navarro J. F., Frenk C. S., White S. D. M., 1996, *ApJ*, 462, 563
- Navarro J. F., Frenk C. S., White S. D. M., 1997, *ApJ*, 490, 493
- Navarro J. F., Helmi A., Freeman K. C., 2004, *ApJ*, 601, L43
- Norris J. E., Ryan S. G., 1991, *ApJ*, 380, 403
- Ojha D. K., 2001, *MNRAS*, 322, 426
- Pardi M. C., Ferrini F., Matteucci F., 1995, *ApJ*, 444, 207

- Peebles P. J. E., 1980, *The large-scale structure of the universe*. Princeton, NJ, Princeton University Press, 1980. 435 p.
- Pohlen M., Balcells M., Lütticke R., Dettmar R.-J., 2004, *A&A*, 422, 465
- Pohlen M., Dettmar R.-J., Lütticke R., Schwarzkopf U., 2000, *A&AS*, 144, 405
- Press W. H., Teukolsky S. A., Vetterling W. T., Flannery B. P., 1992, *Numerical recipes in C. The art of scientific computing*. Cambridge: University Press, —c1992, 2nd ed.
- Quinn P. J., 1984, *ApJ*, 279, 596
- Quinn P. J., Goodman J., 1986, *ApJ*, 309, 472
- Quinn P. J., Hernquist L., Fullagar D. P., 1993, *ApJ*, 403, 74
- Robertson B., Bullock J. S., Cox T. J., Di Matteo T., Hernquist L., Springel V., Yoshida N., 2006, *ApJ*, 645, 986
- Robin A. C., Haywood M., Creze M., Ojha D. K., Bienayme O., 1996, *A&A*, 305, 125
- Romano-Diaz E., Faltenbacher A., Jones D., Heller C., Hoffman Y., Shlosman I., 2006, *ApJ*, 637, L93
- Sadler E. M., Gerhard O. E., 1985, *MNRAS*, 214, 177
- Schweizer F., 1980, *ApJ*, 237, 303
- Schweizer F., Seitzer P., 1988, *ApJ*, 328, 88
- Sellwood J. A., 1987, *ARA&A*, 25, 151
- Sellwood J. A., Nelson R. W., Tremaine S., 1998, *ApJ*, 506, 590
- Seth A. C., Dalcanton J. J., de Jong R. S., 2005, *AJ*, 130, 1574
- Soubiran C., Bienaymé O., Siebert A., 2003, *A&A*, 398, 141
- Soubiran C., Girard P., 2005, *A&A*, 438, 139
- Spitzer L. J., 1942, *ApJ*, 95, 329
- Springel V., 2005, *MNRAS*, 364, 1105
- Springel V., White S. D. M., 1999, *MNRAS*, 307, 162
- Stoeck F., 2003, PhD thesis, Max-Planck-Institut für Astrophysik, Germany
- Toomre A., 1964, *ApJ*, 139, 1217
- Tormen G., 1997, *MNRAS*, 290, 411
- Tóth G., Ostriker J. P., 1992, *ApJ*, 389, 5
- Tsikoudi V., 1979, *ApJ*, 234, 842
- Vallenari A., Pasetto S., Bertelli G., Chiosi C., Spagna A., Lattanzi M., 2006, *A&A*, 451, 125
- van der Kruit P. C., 1984, *A&A*, 140, 470
- van der Kruit P. C., Searle L., 1981a, *A&A*, 95, 105
- van der Kruit P. C., Searle L., 1981b, *A&A*, 95, 116
- van Dokkum P. G., Peletier R. F., de Grijs R., Balcells M., 1994, *A&A*, 286, 415
- Velázquez H., White S. D. M., 1999, *MNRAS*, 304, 254
- Vitvitska M., Klypin A. A., Kravtsov A. V., Wechsler R. H., Primack J. R., Bullock J. S., 2002, *ApJ*, 581, 799
- Walker I. R., Mihos J. C., Hernquist L., 1996, *ApJ*, 460, 121
- Wechsler R. H., Bullock J. S., Primack J. R., Kravtsov A. V., Dekel A., 2002, *ApJ*, 568, 52
- Wilkinson A., Prieur J.-L., Lemoine R., Carter D., Malin D., Sparks W. B., 2000, *MNRAS*, 319, 977
- Wyse R. F. G., Gilmore G., Norris J. E., Wilkinson M. I., Kleyna J. T., Koch A., Evans N. W., Grebel E. K., 2006, *ApJ*, 639, L13
- Yoachim P., Dalcanton J. J., 2005, *ApJ*, 624, 701
- Yoachim P., Dalcanton J. J., 2006, *AJ*, 131, 226
- Zhao D. H., Jing Y. P., Mo H. J., Börner G., 2003, *ApJ*, 597, L9
- Zhao D. H., Mo H. J., Jing Y. P., Börner G., 2003, *MNRAS*, 339, 12